Overview of the CHarring Ablator Response (*CHAR*) Code

Adam J. Amar,* A. Brandon Oliver,* Benjamin S. Kirk,* and Giovanni Salazar*

NASA Lyndon B. Johnson Space Center

2101 NASA Parkway, Houston, TX, 77058

Justin Droba*

NASA Lyndon B. Johnson Space Center, Houston, TX, 77058

JSC Engineering, Technology, and Science (JETS): Jacobs Technology and HX5, LLC

An overview of the capabilities of the *CH*arring *A*blator *R*esponse (*CHAR*) code is presented. *CHAR* is a one-, two-, and three-dimensional unstructured continuous Galerkin finite-element heat conduction and ablation solver with both direct and inverse modes. Additionally, *CHAR* includes a coupled linear thermoelastic solver for determination of internal stresses induced from the temperature field and surface loading. Background on the development process, governing equations, material models, discretization techniques, and numerical methods is provided. Special focus is put on the available boundary conditions including thermochemical ablation and contact interfaces, and example simulations are included. Finally, a discussion of ongoing development efforts is presented.

Nomenclature

α	thermal diffusivity $(\mathrm{m}^2/\mathrm{sec})$ or coefficient of thermal expansion (K^{-1}) or absorptivity
$\alpha_t, \beta_t, \gamma_t$	temporal finite-difference weights (sec^{-1})
β	extent of reaction (degree of char)
$\boldsymbol{f}$	external force vector $(\mathrm{N}/\mathrm{m}^3)$
$\boldsymbol{U}$	vector of discrete unknowns
$\boldsymbol{u}$	displacement vector (m)
$\boldsymbol{v}$	velocity vector $(\mathrm{m}/\mathrm{sec})$
$\boldsymbol{x}$	vector of coordinates (m)
Δh	characteristic mesh length scale (m)
Δt	time step (sec)
$\dot{\omega}$	mass source $(\mathrm{kg}/\mathrm{m}^3 \cdot \mathrm{sec})$
$\dot{m}$	mass flux $(\mathrm{kg}/\mathrm{m}^2 \cdot \mathrm{sec})$
$\dot{Q}$	energy source $(\mathrm{W}/\mathrm{m}^3)$
$\dot{q}$	heat flux $(\mathrm{W}/\mathrm{m}^2)$
Γ	domain boundary (m^2) or volume fraction in virgin material
γ_P	parameters for defining gas flow contact model stability parameter $(\mathrm{m}^2/\mathrm{sec})$ and (sec)
$\hat{\boldsymbol{n}}$	unit normal vector
κ	permeability (m^2)
λ	Lamé's first parameter (Pa) or blowing reduction parameter
$\mathcal{R}$	residual
μ	dynamic viscosity $(\mathrm{Pa} \cdot \mathrm{sec})$ or Lamé's second parameters (Pa)
ν	Poisson's ratio
Ω	domain volume (m^3)
ϕ	porosity

*Applied Aeroscience and CFD Branch, Member AIAA.

ψ	basis function
ρ	density $(\mathrm{kg}/\mathrm{m}^3)$
σ	Stefan-Boltzmann constant $(\mathrm{W}/\mathrm{m}^2\cdot\mathrm{K}^4)$ or stress (Pa)
σ_P	gas flow contact model stability parameter $(\mathrm{m}/\mathrm{sec})$ and $(\mathrm{sec}/\mathrm{m})$
σ_T	thermal contact model stability parameter $(\mathrm{W}/\mathrm{m}^2\cdot\mathrm{K})$
τ	shear stress (Pa)
$\tilde{\boldsymbol{\alpha}}$	coefficient of thermal expansion tensor (K^{-1})
$\tilde{\boldsymbol{\sigma}}$	shear stress tensor (Pa)
$\tilde{\boldsymbol{\varepsilon}}$	mechanical strain tensor
$\tilde{\boldsymbol{C}}$	rotation matrix to shift coordinate reference frame
$\tilde{\boldsymbol{K}}$	stiffness tensor (Pa)
$\tilde{\boldsymbol{\kappa}}$	permeability tensor (m^2)
$\tilde{\boldsymbol{k}}$	thermal conductivity tensor $(\mathrm{W}/\mathrm{m}\cdot\mathrm{K})$
ε	emissivity
A	element face area (m^2)
b	Klinkenberg parameter (Pa)
B'	non-dimensional mass flux
C	specific heat $(\mathrm{J}/\mathrm{kg}\cdot\mathrm{K})$
C_H	convective heat transfer Stanton number
DE	discretization error
E	activation energy (J/kg) or Young's modulus (Pa)
e_o	total internal energy (J/kg)
H	convective heat transfer coefficient $(\mathrm{W}/\mathrm{m}^2\cdot\mathrm{K})$
h	enthalpy (J/kg)
H_c	contact conductance coefficient $(\mathrm{W}/\mathrm{m}^2\cdot\mathrm{K})$
h_o	total enthalpy (J/kg)
k	pre-exponential factor (sec^{-1}) or roughness height (m) or thermal conductivity $(\mathrm{W}/\mathrm{m}\cdot\mathrm{K})$
k^+	non-dimensional roughness height
m	reaction order
N	number of nodes
nc	number of components
P	pressure (Pa)
p	temporal order of accuracy
q	spatial order of accuracy
R	gas constant $(\mathrm{J}/\mathrm{kg}\cdot\mathrm{K})$
S	interface boundary (m^2)
T	temperature (K)
t	time (sec)
u	displacement (m) or velocity $(\mathrm{m}/\mathrm{sec})$
V	element volume (m^3)
v	test function
y	effective mass fractions in solid
DoF	acronym for degree of freedom
PDE	acronym for partial differential equation
TC	abbreviation for thermocouple
TPS	acronym for thermal protection system

Subscripts and Superscripts

∞	denotes far-field state
ν	iteration index
c	quantity of the char
$cond$	denotes conduction
e	quantity at boundary layer edge
g	quantity of the gas
h	denotes finite-dimensional approximation
i	component index

m	quantity of the mesh
n	time index
o	denotes total quantity or initial value
r	denotes recovery state
rad	denotes radiation
s	quantity of the solid
$spec$	denotes user-specified quantity
v	quantity of the virgin or denotes Voigt notation
w	quantity of gases adjacent to the wall

I. Introduction

Ablation is the phenomenon by which a material sacrifices mass through mechanical and thermochemical processes such as spallation, sublimation, oxidation, nitridation, and other reactions in order to expel energy from the material. Ablative materials (ablators) are often used in thermal protection system (TPS) applications such as fire protection, rocket nozzle linings, launch vehicle heatshields, entry vehicle heatshields, and hypersonic cruise vehicle heatshields. Ablators have high temperature capability, and are typically used when the aerothermodynamic environments are too high for reusable TPS materials, such as those used on the Space Shuttle Orbiter. Additionally, ablators are typically more chemically and thermally complex than reusable TPS materials.

In general, there are two types of ablators: charring and surface (non-charring) ablators. A generalized schematic of a charring ablator can be seen in Figure 1. Initially, the material starts out as a virgin composite, which is usually composed of a fibrous material injected with a resin that fills the pore space and strengthens the composite. As heat is transferred into the material, constituents of both the resin and fibrous material can pyrolyze, and the resulting gases percolate away from the decomposition zone toward the surface and eventually out of the material. The fully pyrolyzed material that remains is called char, which has a higher porosity and permeability than the virgin composite. The pyrolysis process is typically endothermic, and the gases are expelled from the surface, which mitigates heat transfer to the substructure. Additionally, pyrolysis gas injection into the boundary layer will reduce the convective heat flux incident on the surface. As the heat flux is increased, chemical reactions with boundary layer gases begin to ablate the surface char, and mass is removed, thereby thinning the material. Char layers typically have low conductivity with high emissivity so that a high surface temperature can be maintained and a significant portion of the incident heat flux can be reradiated. Surface ablators are a simplification of charring ablators in that they only undergo the surface reaction and mass loss process, while they are thermochemically stable in-depth.

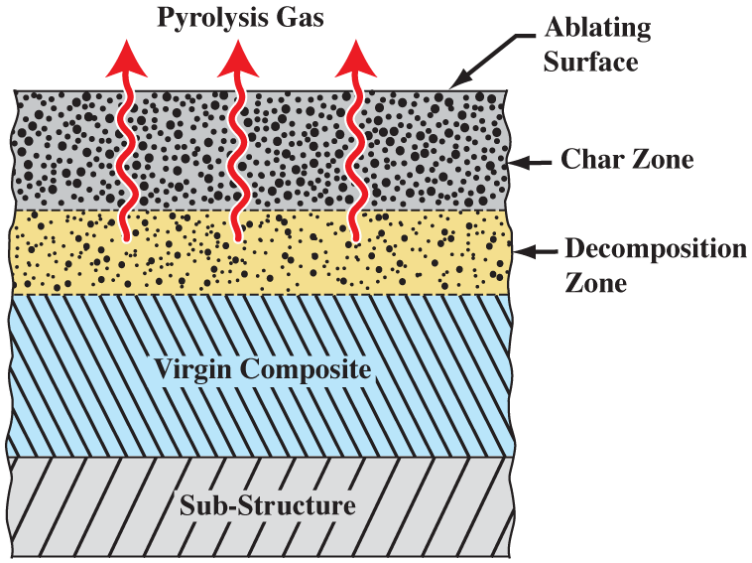

Figure 1. In-depth schematic of a charring (pyrolyzing) ablator.

Reliable predictions of the performance of TPS is critical in the design of such systems. This is typically done

through testing and computer modeling. For decades, design engineers have relied on numerical heat transfer solutions for the highest fidelity thermal response predictions. Numerical methods were first applied to ablative materials in the 1960s during intercontinental ballistic missile and spacecraft development efforts.

This document outlines the physical and numerical models that are implemented in the *CH*arring *A*blator *R*esponse (*CHAR*) code. *CHAR* is a one-, two-, and three-dimensional heat transfer, ablation, and porous flow simulation tool with both direct and inverse solver modes. It uses a continuous Galerkin finite-element spatial discretization with an Euler implicit time discretization and solves the governing equations coupled and implicit with a full-matrix (whole domain) linear system solver. *CHAR*'s primary purpose is to perform engineering analysis for design work. Consequently, the developers have attempted to balance fidelity with speed such that it can be useful in typical engineering design processes. Consequently, *CHAR* employs a macroscale model that leverages volume-averaged assumptions, and it does not have the potential fidelity of microscale models such as those implemented in PATO.[1]

An exhaustive literature review detailing the history of ablation modeling would be prolix and has been done (at least in parts) in other publications. However, the development of *CHAR* was strongly influenced by previous and ongoing modeling efforts including: CMA,[2] Chen and Milos,[3–5] Dec,[6] Blackwell,[7,8] Martin,[9–11] April et al.,[12,13] and Amar.[14]

The intent of this document is to provide an overview of the modeling capabilities implemented in *CHAR*. In an attempt to provide broad coverage, many low-level details are omitted especially in cases where additional references are provided. Notably, details of the inverse algorithm are provided by Oliver,[15] surface-to-surface radiation exchange models are described by Salazar,[16], mesh motion boundary conditions are given by Droba,[17] and verification strategy and results are provided by Amar et al.[18]

II. Software Development Approach

II.A. Code Architecture

To expedite the software development process, the development team has chosen to take advantage of pre-existing, high quality, and freely available software libraries to avoid duplicating the efforts of others. Consequently, the *CHAR* program can be thought of as an ablation and heat transfer physics wrapper around a hierarchy of libraries that aid in the solution and data management processes. The primary software packages included in *CHAR* are outlined in Figure 2, and there are additional libraries that the noted libraries rely on for the functionality in *CHAR*. The majority of the physics and application-dependent code is in the top-level routines denoted by the *CHAR* bubble. This includes simulation management, initialization, calls to library functions, matrix assembly routines for element-level integration, boundary condition application, and material property data structures and look-up routines. Those routines comprised the bulk of the development effort for the current study.

Eigen[19] is a library for linear algebra including: matrix/vector math, numerical solvers, and other related algorithms. It is primarily used in *CHAR* for its matrix and vector data structures and solutions to small linear systems.

Cantera[20] is a collection of object-oriented software tools for problems involving chemical kinetics, thermodynamics, and transport processes. For *CHAR*, it is used to calculate thermodynamic state properties and transport properties for gaseous mixtures in equilibrium. It is used for both the in-depth gas mixture and the environment gas mixture at surface conditions. Since repetitive calls to the equilibrium calculator can get expensive over the course of a simulation, Cantera is only used in the beginning of a simulation to build the required data tables over a range of relevant conditions for the problem. Subsequently, *CHAR* interpolates in these data tables to determine gas properties.

The workhorse for *CHAR* is the `libMesh` finite-element library, which is developed at NASA Johnson Space Center and the University of Texas at Austin with many other contributors around the world.[21] `libMesh` performs nearly all of the physics independent tasks of the software and can be thought of as the framework on which the physics-dependent application code is built. While the functions of `libMesh` within *CHAR* are many, the notable functions include linear system data management, mesh data management, parallel communication, finite-element utilities that streamline integration, and adaptive mesh refinement. `libMesh` also provides user-transparent interfaces to the Portable, Extensible Toolkit for Scientific Computation (PETSc) library,[22] which solves the assembled linear system, and METIS,[23] which provides the domain decomposition for parallel execution.

II.B. Software Verification

The *CHAR* development process has included an extensive verification effort to improve confidence in the software's functionality. Software verification is the mathematical exercise of proving that the model equations and numerical methods have been correctly implemented in the software, not to be confused with software validation which provides

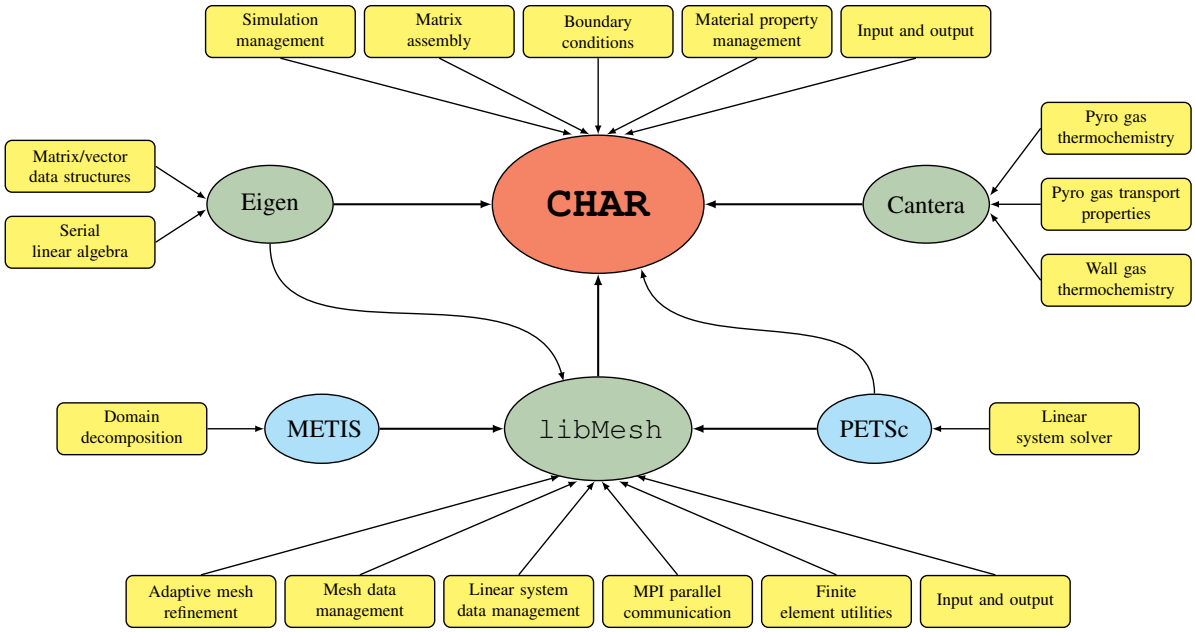

Figure 2. *CHAR* software architecture.

evidence that the correct equations have been chosen to solve the physical problem of interest. Verification includes proving that the spatial and temporal integration techniques and the nonlinear solvers give the desired orders of convergence. While verification studies should be performed for every term in the governing equations, all boundary conditions, and all modeling options, there is some practical limit to how rigorously a developer can verify a code given that most software of this nature is developed in an environment where sooner than later practical problems need to be solved for engineering design and analysis.

Verification exercises are typically done by generating solutions on successively refined space or time meshes for problems with known exact solutions. Examining the discretization error, DE, as the mesh is refined shows the orders of accuracy of the model as implemented.

$$DE = a\Delta t^p + b\Delta h^q + (\text{higher order terms}) \tag{1}$$

where a and b are constants, Δt is the time step, Δh is the characteristic mesh spacing, p is the temporal order of accuracy, and q is the spatial order of accuracy. The general verification approach for *CHAR* is outlined in Amar et al.,[18] where the verification of the fixed-mesh terms in the governing equations are demonstrated. Typically, the spatial and temporal orders of accuracy are independently verified, but an approach for simultaneously verifying the spatial and temporal orders of accuracy is described therein. In general, the two approaches that are used to verify *CHAR* are through analytic solutions and manufactured solutions[24,25] to the governing equations.

III. Governing Equations

CHAR solves the governing equations for heat conduction and gas flow through decomposing porous media in one, two, or three dimensions. In general, this would include

- Continuity equations for each of the chemically reacting gaseous species resulting from flowfield ingestion and pyrolysis gas generation through in-depth decomposition
- Momentum equations accounting for transport through porous media
- Energy equations for both the solid and gas phases
- Solid mass conservation equations for progression of pyrolysis

However, *CHAR* employs several simplifying assumptions to reduce the equation set to be more amenable for engineering application and design analyses. These assumptions include

- Flowfield gases are not allowed to penetrate the surface. Consequently, all the gas inside the porous medium is generated through pyrolysis.
- Pyrolysis gases do not react with or condense on the porous material.
- Pyrolysis gas diffusion is neglected such that the elemental composition of the gas is constant.
- All ablation occurs at the surface, and volume ablation effects are neglected.
- The solid and gas are assumed to be at the same temperature.
- The gas is assumed to be a mixture of perfect gases in chemical equilibrium.
- The momentum equations can be sufficiently represented by the steady form of Darcy's law.

Under these assumptions, the governing equations for a moving mesh simplify to

$$\begin{aligned} \text{Energy:}\quad & \left.\frac{\partial(\rho e_o)}{\partial t}\right|_{node} - \boldsymbol{\nabla}\cdot\left(\tilde{\boldsymbol{k}}\boldsymbol{\nabla}T\right) + \boldsymbol{\nabla}\cdot\left(\phi\rho_g h_{o_g}\boldsymbol{v}_g\right) - \boldsymbol{v}_m\cdot\boldsymbol{\nabla}(\rho e_o) - \dot{Q} = 0 \\ \text{Gas Mass:}\quad & \left.\frac{\partial(\phi\rho_g)}{\partial t}\right|_{node} - \dot{\omega}_g + \boldsymbol{\nabla}\cdot(\phi\rho_g\boldsymbol{v}_g) - \boldsymbol{v}_m\cdot\boldsymbol{\nabla}(\phi\rho_g) = 0 \end{aligned} \tag{2}$$

where the $node$ subscript denotes conservation with respect to a constant location in the moving coordinate frame (such as a node in the moving mesh) and Darcy's law defines the velocity field by

$$\boldsymbol{v}_g = -\frac{\tilde{\boldsymbol{\kappa}}}{\phi\mu}\boldsymbol{\nabla}P \tag{3}$$

Additionally, the solid mass conservation equation, given by

$$\frac{\partial\rho_s}{\partial t} = \dot{\omega}_s = -\dot{\omega}_g \tag{4}$$

is solved in a stationary reference frame and treated as a constitutive relation when defining the temporal derivative in the energy equation.

IV. Numerical Methods

IV.A. Finite-Element Formulation

In order to develop the finite-element equations, Galerkin weak statements can be developed for the energy and gas mass conservation equations in Eqn. (2) by first multiplying each by a suitable test function, v, and integrating over the domain, Ω, while integrating the appropriate terms by parts to give the natural boundary condition terms. The weak statement is then: Find ρe_o and $\phi\rho_g \in H^1$ such that

$$\begin{aligned} \int_\Omega \left[v\frac{\partial(\rho e_o)}{\partial t} + \boldsymbol{\nabla}v\cdot\left(\tilde{\boldsymbol{k}}\boldsymbol{\nabla}T\right) - \boldsymbol{\nabla}v\cdot\left(\phi\rho_g h_{o_g}\boldsymbol{v}_g\right) - v\boldsymbol{v}_m\cdot\boldsymbol{\nabla}(\rho e_o) - v\dot{Q}\right]d\Omega \\ + \oint_\Gamma \left(vh_{o_g}\dot{m}_g + v\dot{q}_{cond_s}\right)d\Gamma = 0 \quad \forall v \in H^1 \end{aligned} \tag{5}$$

$$\int_\Omega \left(\frac{\partial(\phi\rho_g)}{\partial t}v - \boldsymbol{\nabla}v\cdot(\phi\rho_g\boldsymbol{v}_g) - v\boldsymbol{v}_m\cdot\boldsymbol{\nabla}(\phi\rho_g) + \dot{\omega}_s v\right)d\Omega + \oint_\Gamma v\dot{m}_g d\Gamma = 0 \quad \forall v \in H^1 \tag{6}$$

where the boundary mass flux due to gas convection is

$$\dot{m}_g = (\phi\rho_g)\,\boldsymbol{v}_g\cdot\hat{\boldsymbol{n}} \tag{7}$$

and the boundary heat flux is

$$\dot{q}_{cond_s} = -\tilde{\boldsymbol{k}}\boldsymbol{\nabla}T\cdot\hat{\boldsymbol{n}} \tag{8}$$

The finite-element approximation to Eqns. (5) and (6) can be reached by expanding the independent variables and test functions in terms of a finite dimensional basis

$$(\rho e_o)_h(\boldsymbol{x}) = \sum_{j=1}^{N} (\rho e_o)_j \psi_j(\boldsymbol{x}) \tag{9}$$

$$(\phi\rho_g)_h(\boldsymbol{x}) = \sum_{j=1}^{N} (\phi\rho_g)_j \psi_j(\boldsymbol{x}) \tag{10}$$

$$T_h(\boldsymbol{x}) = \sum_{j=1}^{N} T_j \psi_j(\boldsymbol{x}) \tag{11}$$

$$P_h(\boldsymbol{x}) = \sum_{j=1}^{N} P_j \psi_j(\boldsymbol{x}) \tag{12}$$

$$v_h(\boldsymbol{x}) = \sum_{i=1}^{N} v_i \psi_i(\boldsymbol{x}) \tag{13}$$

where the subscript h is introduced to denote a finite dimensional approximation. The unknowns in the system are chosen to be the nodal temperatures and pressures, T_j and P_j. Since the unknowns are not functions of $\boldsymbol{x}$, the partial differential equation system is reduced to an ordinary differential equation system in which the temporal derivatives can be defined as

$$\frac{\partial(\rho e_o)_h}{\partial t} = \sum_{j=1}^{N} \frac{d(\rho e_o)_j}{dt} \psi_j(\boldsymbol{x}) \tag{14}$$

$$\frac{\partial(\phi\rho_g)_h}{\partial t} = \sum_{j=1}^{N} \frac{d(\phi\rho_g)_j}{dt} \psi_j(\boldsymbol{x}) \tag{15}$$

Since the equation system should be satisfied for all combinations of nodal shape function coefficients, v_i, their choice is arbitrary as long as a unique combination is chosen for each node. In typical finite-element fashion, the coefficients are chosen to be $v_i = \delta_{il}$ for the l^{th} nodal equation. Consequently, the nodal residual equations resulting from Eqns. (5) and (6) can now be written as

$$\begin{aligned} &\int_\Omega \psi_i \frac{\partial(\rho e_o)_h}{\partial t} d\Omega + \int_\Omega \boldsymbol{\nabla}\psi_i \cdot \boldsymbol{k}\boldsymbol{\nabla} T_h d\Omega - \int_\Omega (\phi\rho_g)_h h_{o_g} \boldsymbol{\nabla}\psi_i \cdot \boldsymbol{v}_g d\Omega \\ &- \int_\Omega \psi_i \boldsymbol{v}_m \cdot \boldsymbol{\nabla}(\rho e_o)_h d\Omega + \oint_\Gamma \psi_i \dot{q}_{cond_s} d\Gamma + \oint_\Gamma \psi_i h_{o_g} \dot{m}_g d\Gamma - \int_\Omega \psi_i \dot{Q} d\Omega = 0 \end{aligned} \tag{16}$$

and

$$\int_\Omega \psi_i \frac{\partial(\phi\rho_g)_h}{\partial t} d\Omega - \int_\Omega (\phi\rho_g)_h \boldsymbol{\nabla}\psi_i \cdot \boldsymbol{v}_g d\Omega - \int_\Omega \psi_i \boldsymbol{v}_m \cdot \boldsymbol{\nabla}(\phi\rho_g)_h d\Omega + \oint_\Gamma \psi_i \dot{m}_g d\Gamma + \int_\Omega \psi_i \dot{\omega}_s d\Omega = 0 \tag{17}$$

for i = 1,2,...,N.

The residual equations are numerically integrated with either Gaussian or trapezoidal quadrature depending on the user's preference. First order Lagrangian shape functions are used, which gives a second order accurate spatial discretization. Supported element types include:

- 1D: 2-DoF bar elements
- 2D: 4-DoF quadrilateral and 3-DoF triangle elements
- 3D: 8-DoF hexahedron, 4-DoF tetrahedron, 6-DoF prism, and 5-DoF pyramid elements

IV.B. Time Discretization

The semidiscrete weak form of the system given by Eqns. (16) and (17) is discretized in time using backward finite-difference schemes. Both first- and second-order accurate schemes may be derived from Taylor series expansions in time about $\boldsymbol{U}_{n+1}$ as outlined by Kirk[26] to give

$$\frac{\partial \boldsymbol{U}_{n+1}}{\partial t} = \alpha_t \boldsymbol{U}_{n+1} + \beta_t \boldsymbol{U}_n + \gamma_t \boldsymbol{U}_{n-1} + \mathcal{O}\left(\Delta t_{n+1}^p\right) \tag{18}$$

where the weights are given for $p = 1$ and $p = 2$ in Table 1.

Table 1. First- and second-order accurate time discretization coefficients.

p	α_t	β_t	γ_t
1	$\frac{1}{\Delta t_{n+1}}$	$\frac{-1}{\Delta t_{n+1}}$	0
2	$-\beta_t - \gamma_t$	$-\left[\frac{1}{\Delta t_{n+1}} + \frac{1}{\Delta t_n}\right]$	$\frac{\Delta t_{n+1}}{\Delta t_n(\Delta t_{n+1}+\Delta t_n)}$

The resulting temporal derivatives are given by

$$\frac{d\left(\rho e_o\right)_j}{dt} = \alpha_t \left(\rho e_o\right)_j^{n+1} + \beta_t \left(\rho e_o\right)_j^{n} + \gamma_t \left(\rho e_o\right)_j^{n-1} \tag{19}$$

and

$$\frac{d\left(\phi \rho_g\right)_j}{dt} = \alpha_t \left(\phi \rho_g\right)_j^{n+1} + \beta_t \left(\phi \rho_g\right)_j^{n} + \gamma_t \left(\phi \rho_g\right)_j^{n-1} \tag{20}$$

which can be substituted into Eqns. (14) and (15) respectively.

IV.C. Linearization

Through the iteration process, the nodal residual equations will be driven to machine zero so that the nonlinear governing equations are satisfied in a discrete sense. The DoFs are chosen to be nodal values of T and P, which is an update from the earlier version of *CHAR* described in Amar et al.[18] To aid in the iterative process, it is necessary to linearize the residual equations in iteration space. This will be done according to a Taylor-series expansion

$$\mathcal{R}_i^{\nu+1} = \mathcal{R}_i^{\nu} + \sum_{j=1}^{N} \left\{ \left.\frac{\partial \mathcal{R}_i}{\partial T_j}\right|^{\nu} \Delta T_j + \left.\frac{\partial \mathcal{R}_i}{\partial P_j}\right|^{\nu} \Delta P_j \right\} + \text{higher order terms} \tag{21}$$

where the superscript ν has been introduced to denote iteration level and

$$\Delta T_j = T_j^{\nu+1} - T_j^{\nu} \tag{22}$$

and

$$\Delta P_j = P_j^{\nu+1} - P_j^{\nu} \tag{23}$$

Keep in mind that the Jacobian terms, $\frac{\partial \mathcal{R}_i}{\partial ()_j}$, are only nonzero if nodes i and j share an element.

Since the intent of *CHAR* is to allow for easy addition of new physical models, the Jacobians will not be derived analytically yet they will be calculated exactly (to machine precision) using the complex-step method as described in Amar et al.[18] and originally introduced by Lyness.[27,28] The residuals can be expanded according to a Taylor-series in independent variable space about a point $[T_j, P_j]$. For example, the expansion in temperature space with complex step, $i\Delta T$, is

$$\mathcal{R}\left[T_j + i\Delta T_j, P_j\right] = \mathcal{R}\left[T_j, P_j\right] + i\frac{\partial \mathcal{R}}{\partial T_j}\left(\Delta T_j\right) - \frac{1}{2}\frac{\partial^2 \mathcal{R}}{\partial T_j^2}\left(\Delta T_j\right)^2 - \frac{i}{6}\frac{\partial^3 \mathcal{R}}{\partial T_j^3}\left(\Delta T_j\right)^3 + \text{ higher order terms} \tag{24}$$

Now looking at just the imaginary part and ignoring the higher order terms gives

$$Im\left\{\mathcal{R}\left[T_j + i\Delta T_j, P_j\right]\right\} = \frac{\partial \mathcal{R}}{\partial T_j}\Delta T_j - \frac{1}{6}\frac{\partial^3 \mathcal{R}}{\partial T_j^3}\left(\Delta T_j\right)^3 \tag{25}$$

Solving for the first derivative gives the Jacobian terms

$$\frac{\partial \mathcal{R}}{\partial T_j} = \frac{Im\left\{\mathcal{R}\left[T_j + i\Delta T_j, P_j\right]\right\}}{\Delta T_j} + \mathcal{O}\left[\left(\Delta T_j\right)^2\right] \tag{26}$$

This process can be repeated for each independent variable. The proper choice for the perturbation steps is not immediately obvious from looking at the equations, but as demonstrated in Amar et al.,[18] picking a good value to obtain exact Jacobians is easily accomplished in practice. Since after the residual is calculated there are no addition or subtraction operations in Eqn. 26 to introduce truncation errors, choosing a very small value for the perturbation step, such as $\Delta T_j = T_j \times 10^{-100}$, is sufficient.

V. Material Model

The material model is an extension of the CMA model developed by Moyer and Rindal.[2] It is assumed that all the pores are interconnected, and therefore pyrolysis gases occupy all of the pore space and are free to flow through it. Consequently, the density of the solid/gas system is described by

$$\rho = \phi\rho_g + \rho_s \tag{27}$$

where the solid density is a bulk density, the gas density is with respect to the space the gas occupies (pore space), and the porosity is equal to the gas volume fraction. In terms of units, Eqn. (27) can be expressed as

$$\overbrace{\frac{\text{[total mass]}}{\text{[total vol]}}}^{\rho} = \overbrace{\frac{\text{[pore vol]}}{\text{[total vol]}}}^{\phi}\overbrace{\frac{\text{[gas mass]}}{\text{[pore vol]}}}^{\rho_g} + \overbrace{\frac{\text{[solid mass]}}{\text{[total vol]}}}^{\rho_s} \tag{28}$$

The solid material is modeled as a mixture of components each with their own rate law governing its decomposition.

$$\rho_s = \sum_{i=1}^{nc} \Gamma_i \rho_{s_i} \tag{29}$$

It is assumed that the solid does not change volume due to thermal expansion, and therefore the total volume is constant. It is important to note that the solid description in Eqn. (29) is only a modeling assumption, and the solid is not truly comprised of nc components, species, or distinguishable materials. Taking the temporal derivative of Eqn. (29) gives the solid decomposition rate in terms of component decomposition rates.

$$\frac{\partial \rho_s}{\partial t} = \dot{\omega}_s = \sum_{i=1}^{nc} \Gamma_i \frac{\partial \rho_{s_i}}{\partial t} = \sum_{i=1}^{nc} \Gamma_i \dot{\omega}_{s_i} \tag{30}$$

It is assumed that the decomposition of each component can be described by an Arrhenius relationship of the form

$$\dot{\omega}_{s_i} = -k_i \rho_{v_i} \left(\frac{\rho_i - \rho_{c_i}}{\rho_{v_i}}\right)^{m_i} e^{-E_i/RT} \tag{31}$$

which is in a stationary reference frame. The decomposition kinetics in Eqn. (31) are simplified to ordinary differential equations by treating the temperature constant over a time step as proposed by Moyer and Rindal. They are then treated as a constitutive relation and directly integrated as part of the solution to the energy equation.

Since most thermophysical properties of the solid are only known for the virgin and fully charred states, the intermediate solid is modeled as an interpolated state between virgin and char. This interpolated state is characterized by the extent of reaction (β), or degree of char, given by

$$\beta = \frac{\rho_v - \rho_s}{\rho_v - \rho_c} \tag{32}$$

where the virgin and char bulk densities are known constants. The definition in Eqn. (32) can be rearranged to more clearly describe the interpolated state.

$$\rho_s = (1 - \beta)\,\rho_v + \beta\rho_c \tag{33}$$

Although the virgin and char materials are not distinguishable entities within the intermediate solid, Eqn. (33) reveals that the degree of char represents an effective char volume fraction within the solid. In a similar light, CMA defines an effective virgin mass fraction given by

$$y_v = \frac{\rho_v}{\rho_v - \rho_c}\left(1 - \frac{\rho_c}{\rho_s}\right) \tag{34}$$

which can be related to the extent of reaction through

$$y_v = \frac{\rho_v}{\rho_s}\left(1 - \beta\right) \tag{35}$$

Similarly the char mass fraction is given by

$$y_c = 1 - y_v = \frac{\rho_c}{\rho_s}\beta \tag{36}$$

These effective parameters are used to interpolate between virgin and char thermophysical properties for partially decomposed material.

$$\rho e_o = \left(1 - \beta\right)\rho_v e_v + \beta \rho_c e_c + \phi \rho_g e_{o_g} \tag{37}$$

$$k = y_v k_v + y_c k_c + \phi k_g \tag{38}$$

$$\varepsilon = y_v \varepsilon_v + y_c \varepsilon_c \tag{39}$$

$$\alpha = y_v \alpha_v + y_c \alpha_c \tag{40}$$

Additionally, the porosity and permeability are treated as user-defined functions of degree of char, β. Also, the permeability is treated with a pressure dependence according to the Klinkenberg model.[29]

$$\kappa = \kappa_o\left(1 + \frac{b}{P}\right) \tag{41}$$

Finally, both the thermal conductivity and the permeability can be treated anisotropically.

VI. Mesh Motion

For materials that undergo small deformation, to good approximation, the stress in the material is linearly proportional to its strain. Such materials are said to behave as *linear elastic* materials, and their displacement $\boldsymbol{u}$ under an external force $\boldsymbol{f}$ is described by

$$-\boldsymbol{\nabla}\lambda\left(\boldsymbol{\nabla}\cdot\boldsymbol{u}\right) - \left(\boldsymbol{\nabla}\cdot\mu\boldsymbol{\nabla}\right)\boldsymbol{u} - \boldsymbol{\nabla}\cdot\mu\left(\boldsymbol{\nabla}\boldsymbol{u}\right)^T = \boldsymbol{f} \tag{42}$$

where λ and μ are the Lamé parameters.

A weak formulation can be constructed for Eqn. (42) in the usual way. Multiplying by a suitable test function $\boldsymbol{v}$ and integrating by parts, the weak form is then: Find $\boldsymbol{u} \in H^1$ such that

$$\sum_{k,l}\int_\Omega \lambda\frac{\partial u_l}{\partial x_l}\frac{\partial v_k}{\partial x_k}\,d\Omega + \sum_{k,l}\int_\Omega \mu\frac{\partial u_l}{\partial x_k}\frac{\partial v_l}{\partial x_k}\,d\Omega + \sum_{k,l}\int_\Omega \mu\frac{\partial u_l}{\partial x_k}\frac{\partial v_k}{\partial x_l}\,d\Omega = \sum_k f_k v_k\,d\Omega \tag{43}$$

$\forall \boldsymbol{v} \in H^1$, where the summation indices expand over the number of spatial dimensions in the problem. The finite-element approximation follows immediately by introducing finite dimensional approximations for $\boldsymbol{u}_h$ and $\boldsymbol{v}_h$. It should be emphasized this implementation of the linear elasticity equations is used solely for mesh motion. In this setting, the "material" properties λ and μ can be chosen to tailor the mesh deformation and need not represent the actual material being modeled. In this work, these parameters are fixed at $\lambda = 0$ and $\mu = 1$, but other choices could improve mesh quality for some situations.

The discrete analog of Eqn. (43) is implemented in the *CHAR*. For generality, the form presented in Eqn. (43) is implemented, although it is expected that only the homogeneous ($\boldsymbol{f} \equiv \boldsymbol{0}$) will be of practical interest.

VI.A. Usage Within an Ablation Simulation

Eqn. (42) is steady. Under the assumption that the mesh deformation is *quasi-steady*, it can be applied at each time step within an ablation simulation. The general usage scenario is that the surface displacement is prescribed as a Dirichlet boundary condition along some portion of the boundary, and the resulting nodal displacements within the ablator are determined from Eqn. (42). The mesh nodal coordinates are then updated using these displacements. Furthermore, the mesh nodal location history is stored at two time levels. This location history can be used to compute the "mesh velocity" terms required by *CHAR* via finite-differencing. This procedure is repeated at each time step.

The mesh motion scheme in *CHAR* is explicit. The surface recession distribution is calculated at time level n, then it is applied and held constant at time level $n+1$. For typical ablation problems, the recession rate changes slow enough that this assumption does not greatly impact accuracy while it provides a significant speed-up over a fully implicit approach.

A critical feature of the implementation is to restrict the linear elasticity solve to a subdomain of the mesh. In this approach, the mesh motion will only occur on a subset of the entire computational mesh. This capability is useful when the full simulation includes both ablating and non-ablating components, for example an ablative material mounted to a rigid structure. This feature will be explicitly demonstrated in Section VI.B.

As *CHAR* has been applied to a broader set of moving mesh problems, it has been recognized that the simple boundary conditions first implemented (not described in detail herein) are insufficient for many problems, especially those with large mesh deformations. Consequently, a current effort is focused on developing a suite of generalized and robust boundary conditions for the linear elastic solver associated with the mesh motion algorithm. These boundary conditions and associated example problems are outlined in Droba.[17]

VI.B. Demonstration Case

The example case considers a generic "iso-q" shape characteristic of arcjet stagnation test specimens. This shape is characterized by a blunt "puck" with a radius of curvature equal to its diameter. When exposed to an impinging stream, this shape results in a laminar heat transfer distribution, which is roughly constant over a large portion of the face. A cross-section of a notional iso-q is shown schematically in Figure 3. This case makes use of the ability to restrict mesh

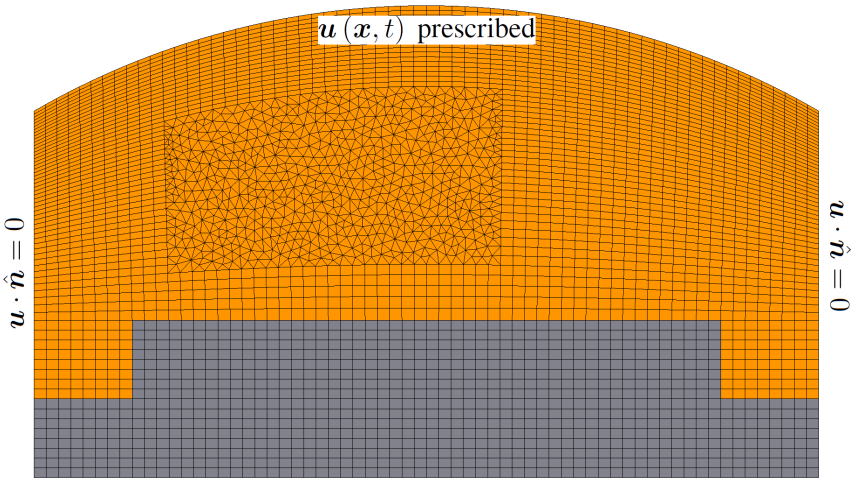

Figure 3. Canonical arcjet iso-q geometry for mesh motion demonstration case.

motion to a specific subdomain. The amber-colored material in this case is assumed to be an ablator, which is allowed to deform. The gray-colored material is treated as fixed. Such a scenario would result from the common test article setup in which an ablative material is bonded to a fixture.

The boundary conditions for this case are shown in the figure. A "sliding" boundary condition is applied on the two vertical sides. Specifically, the displacement is restricted such that $\boldsymbol{u}\cdot\hat{\boldsymbol{n}}=0$. This allows nodes to slide tangential to the boundary, but not move normal to it. The top surface is the surface that in an actual ablation calculation would be exposed to the highest heat flux and therefore experience the most severe recession. In this case, the ablation code would specify the surface displacement at each time step. For demonstration purposes, surface displacement will be

prescribed analytically as

$$u_1 = 0 \tag{44}$$

$$u_2 = -0.01\left(2 + \cos\left(2\pi x\right)\right) \tag{45}$$

where $x \in [-0.5, 0.5]$. This displacement profile is repeatedly applied at the surface in a quasi-static simulation. The displacement history is shown in Figure 4. It is clear from the figure that the mesh motion is properly restricted to the

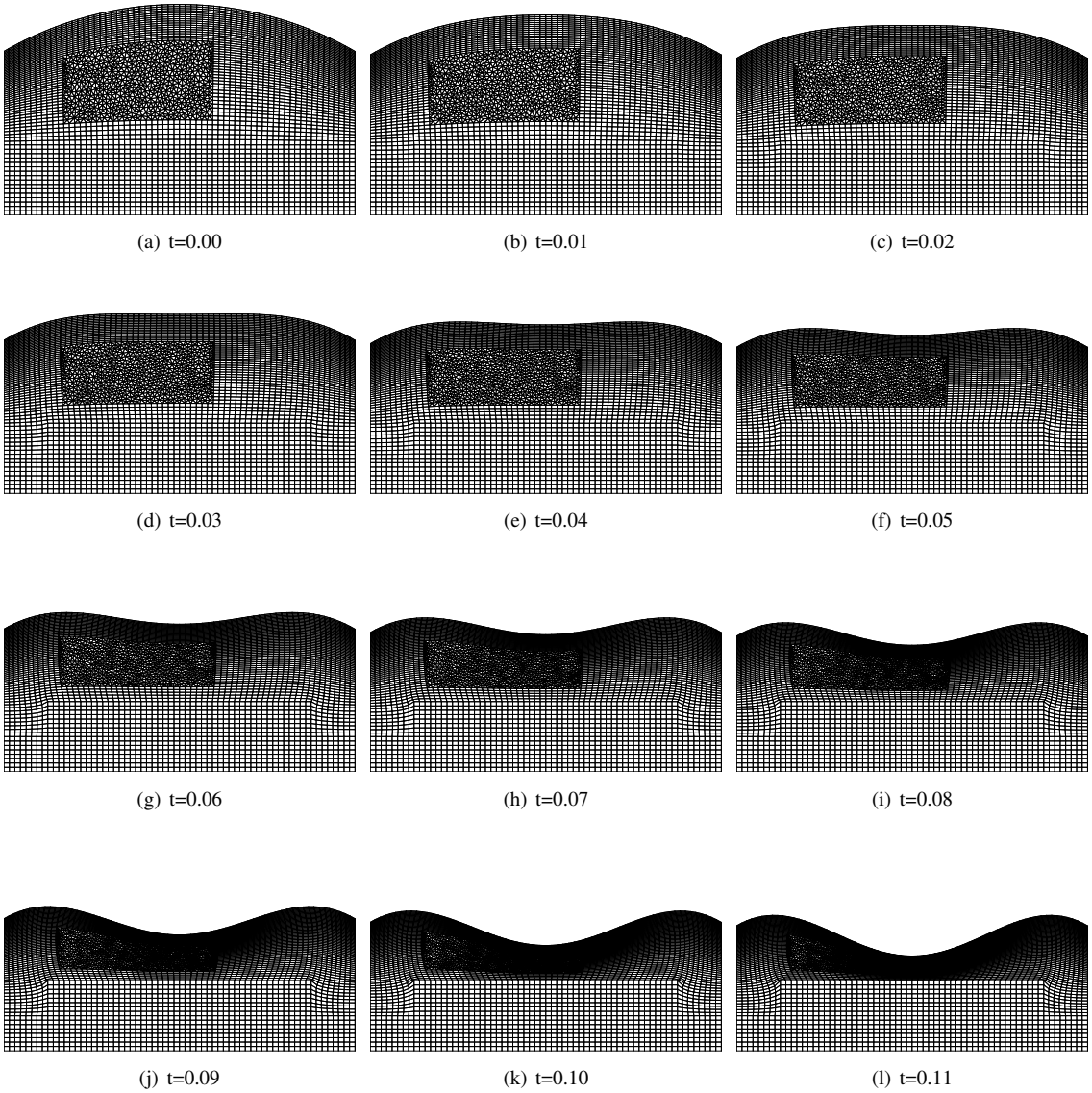

(a) t=0.00 (b) t=0.01 (c) t=0.02

(d) t=0.03 (e) t=0.04 (f) t=0.05

(g) t=0.06 (h) t=0.07 (i) t=0.08

(j) t=0.09 (k) t=0.10 (l) t=0.11

Figure 4. Deformation history for arcjet iso-q geometry.

ablator subdomain.

VII. Boundary Conditions

CHAR has a rich suite of boundary conditions each of which can be treated as temporally and spatially varying. For the energy equation, the options for incident fluxes can be any combination of the following:

- Perfect gas convection: $\dot{q} = H\left(T_r - T_w\right)$
- Real gas convection (Aeroheating): $\dot{q} = \rho_e u_e C_H \left(h_r - h_w\right)$

- Specified heat flux: $\dot{q} = q_{spec}$
- Reradiation: $\dot{q} = \sigma\varepsilon\left(T_\infty^4 - T_w^4\right)$
- Radiation: $\dot{q} = \alpha\dot{q}_{rad}$

In addition, surface-to-surface radiation exchange is available as described by Salazar.[16] Finally for the energy equation, a specified surface temperature (Dirichlet) condition is also available. For the gas mass conservation equation, specified mass flux and specified pressure (Dirichlet) conditions are available. Dirichlet conditions are applied numerically via the penalty boundary method.[30]

For surface recession, melting and thermochemical ablation models are available. The thermochemical ablation model is described in more detail in Section VII.A.

VII.A. Thermochemical Ablation

The fluid ablator interface is governed by mass and energy balances that account for the thermochemical interactions occurring at the surface. Following the film coefficient approach of Moyer and Rindal,[2] the surface energy balance can be expressed as

$$\rho_e u_e C_H \left(h_r - h_w\right) + \alpha\dot{q}_{rad} - \sigma\varepsilon\left(T_w^4 - T_\infty^4\right) - \dot{m}_w h_w + \dot{m}_c h_c + \dot{m}_{g_s} h_g + \dot{q}_{cond_s} = 0 \tag{46}$$

In order to simplify the solutions to the mass and energy balances, non-dimensional mass fluxes are introduced

$$B'_c = \frac{\dot{m}_c}{\rho_e u_e C_H} \tag{47}$$

$$B'_g = \frac{\dot{m}_{g_s}}{\rho_e u_e C_H} \tag{48}$$

and

$$B' = B'_c + B'_g \tag{49}$$

Substituting these new definitions and solving for the conduction flux gives

$$\dot{q}_{cond_s} = -\rho_e u_e C_H \left[\left(h_r - h_w\right) - B' h_w + B'_c h_c + B'_g h_g\right] - \alpha\dot{q}_{rad} + \sigma\varepsilon\left(T_w^4 - T_\infty^4\right) \tag{50}$$

Knowing the temperature and pyrolysis gas mass flux at the surface (from the in-depth solution) and the film coefficient and pressure from the fluid dynamics, the mass balance and surface chemistry problem can be solved to give the solid mass loss rate, $\dot{m}_c$ (or B'_c) and the wall enthalpy, h_w. Solving the mass balance/surface chemistry problem is typically done with an external software package such as ACE[31] or MAT.[32] A multitude of solutions over a bounding range of conditions is typically pre-computed and supplied to the thermal analysis software in tabular form. These surface thermochemistry tables are commonly referred to as "B' tables." For *CHAR*, the independent variables in the B' tables are pressure, B'_g, and temperature. The dependent variables are the wall enthalpy and B'_c. Given the B' tables in addition to the convective, radiation, and reradiation input parameters and the pyrolysis gas information from the in-depth solution, all the information is known to solve for the conduction flux in Eqn. (50).

It should be noted that for typical thermochemical ablation problems, the surface boundary condition for the gas continuity equation is a specified pressure condition, which is known from the fluid dynamics analysis and is already a required input for the surface thermochemistry tables.

VII.A.1. Film Coefficient Corrections

Typically, when performing an uncoupled analysis of an aerothermal and material response problem, the fluid dynamics analysis is performed to provide a heating boundary condition, and the material response simulation takes this fixed boundary condition as input. In reality, the physics of the two problems are coupled because the thermal response impacts the aerothermal environments through wall temperature changes, surface chemical state, mass injection, shape change, and surface roughening. When it is not feasible to perform a coupled analysis to account for these effects, which is most often the case, correction models can be implemented in the material response code. These corrections typically come in the form of film coefficient adjustment models while they leave the recovery state unchanged. Currently, *CHAR* contains film coefficient correction models for both blowing and roughness effects. Although wall temperature correction models are often employed, no such model has been implemented in *CHAR* to date.

BLOWING REDUCTION

Mass injection from the ablator to the boundary layer is known to reduce the convective heating environment to the surface of the ablator. The blowing reduction model in *CHAR* is based on the model presented in Kays.[33] It is derived based on manipulation of the boudary layer equations under Couette flow assumptions, and its applicability is supported by a wealth of test data. It is also the same model implemented in the CMA code.[2]

$$\frac{\rho_e u_e C_H}{\rho_e u_e C_H|_o} = \frac{2\lambda B'_o}{e^{2\lambda B'_o} - 1} \tag{51}$$

where

$$B'_o = \frac{\dot{m}_{g_s} + \dot{m}_c}{\rho_e u_e C_H|_o} = \frac{\dot{m}_w}{\rho_e u_e C_H|_o} \tag{52}$$

where $\rho_e u_e C_H|_o$ is the uncorrected film coefficient supplied as part of the aeroheating boundary condition, and $\dot{m}_w$ is the total mass flux being injected into the fluid stream from the ablator. λ is the blowing reduction parameter, which is dependent on the flow state and can be a tunable parameter for a specific application. Previous experience has shown that suitable choices for λ are

$$\lambda = 0.5 \text{ for laminar flow}$$
$$\lambda = 0.4 \text{ for turbulent flow}$$

Notice that for a given injected mass flux, the blowing reduction is more effective for a laminar flow than it is for a turbulent flow.

ROUGHNESS AUGMENTATION

Surface roughness is known to augment the convective heating environment, particularly in turbulent flow. Typically, roughness augmentation models are based on test data or Reynolds analogy given a corresponding augmentation in skin friction. Consequently, the roughness models implemented in *CHAR* involve a two-step process. The first step is to model the skin friction augmentation given the surface conditions, and the second step is to augment the film coefficient given the skin friction augmentation.

For the skin friction augmentation, a model based on a curve fit of adiabatic flat plate data presented by Reda[34] has been implemented.

$$\frac{\tau_w}{\tau_{w_o}} = 1 + 0.9 \log\left(\frac{k^+}{10}\right) \text{ for } k^+ > 10 \tag{53}$$

where the non-dimensional roughness height is defined as

$$k^+ = \frac{\rho_w \sqrt{\frac{\tau_{w_o}}{\rho_w}} k}{\mu_w} \tag{54}$$

The roughness height, k, and uncorrected shear stress, τ_{w_o}, are supplied to *CHAR* as boundary condition inputs, and the wall density, ρ_w, and wall viscosity, μ_w, are functions of temperature, pressure, and wall gas composition and are tabulated as dependent variables in the surface thermochemistry (B') tables. It is important to note that while the shear stress is corrected to account for the wall gas species resulting from blowing and surface ablation, it is not corrected for changes in the velocity profile due to blowing, which could be significant.

The two available roughness models were developed by Dahm[35] and Finson[36] and are given by

$$\text{Dahm: } \frac{\rho_e u_e C_H}{\rho_e u_e C_H|_o} = 1 + 0.6\left(\frac{\tau_w}{\tau_{w_o}} - 1\right) \tag{55}$$

$$\text{Finson: } \frac{\rho_e u_e C_H}{\rho_e u_e C_H|_o} = \sqrt{\frac{\tau_w}{\tau_{w_o}}} \tag{56}$$

The roughness heating augmentation models should be used with caution because the applicability of these models may not apply to a broad range of roughness types or flow regimes. Consequently, the roughness heating augmentation models available in literature can give a wide range of results. If the luxury exists, development of an application-specific roughness heating augmentation model is advised, which can be easily implemented in the software.

VII.B. Contact Interface Conditions

VII.B.1. Thermal Contact

CHAR has the capability to model thermal contact at interfaces with or without aligned meshes. The two motivations for this capability are contact resistance modeling and eliminating conformal meshing requirements. For non-conformal meshes, the elements at the interfaces are not logically connected in the mesh data. Consequently, algorithms were implemented in *CHAR* to detect element connectivity and book-keep DoF dependencies. While contact modeling has been implemented in the governing equations, *CHAR* cannot currently handle contact interfaces within a moving domain when the mesh motion DoFs on the two sides of the interface depend on each other. This will be addressed in future development.

Two thermal contact models are implemented. The first allows for impedance of heat transfer through a finite contact conductance, H_c.

$$\dot{q} = H_c \left(T^+ - T^-\right) \tag{57}$$

Lower contact conductance values will result in larger differences in temperature at the two sides of the interface, T^+ and T^-. As the contact conductance approaches infinity, the two sides approach thermal equilibrium and perfect thermal contact is recovered. However, very large values for the contact conductance led to numerical issues.

To overcome the numerical issues, a perfect thermal contact model was implemented. Recall the Galerkin weak statement of the energy equation given in Eqn. 5. However, the continuous FEM assumes a continuous solution space, which typically involves a conformal grid. To address this problem, the approach proposed by Dolbow and Harari[37] was followed. In this method, the conditions at the interface are enforced weakly by application of Nitsche's method.[38] To do so, consider a pair of disjointed domains separated by an interface S, which can each have different material properties as shown in Figure 5.

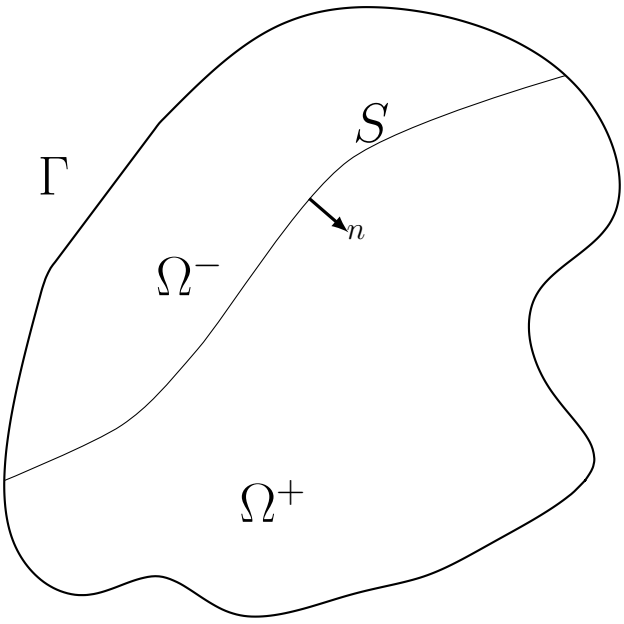

Figure 5. Disjointed domain schematic.

To accommodate this new method, it requires modification to the energy equation's weak statement in Eqn. 5 to include additional terms due to the embedded interface

$$\begin{aligned}\int_\Omega \left[v\frac{\partial(\rho e_o)}{\partial t} + \boldsymbol{\nabla} v \cdot \left(\tilde{\boldsymbol{k}}\boldsymbol{\nabla} T\right) - \boldsymbol{\nabla} v \cdot \left(\phi \rho_g h_{o_g} \boldsymbol{v}_g\right) - v\boldsymbol{v}_m \cdot \boldsymbol{\nabla}(\rho e_o) - v\dot{Q}\right] d\Omega \\ + \oint_\Gamma \left(v h_{o_g} \dot{m}_g + v\dot{q}_{cond_s}\right) d\Gamma - \oint_S [[v]] \left\langle \tilde{\boldsymbol{k}}\boldsymbol{\nabla} T \cdot \hat{\boldsymbol{n}}\right\rangle dS \\ - \oint_S \left\langle \tilde{\boldsymbol{k}}\boldsymbol{\nabla} v \cdot \hat{\boldsymbol{n}}\right\rangle [[T]]\, dS + \oint_S \sigma_T [[v]]\, [[T]]\, dS = 0 \quad \forall v \in H_0^1\end{aligned} \tag{58}$$

where the interface operators are defined as

$$\langle T \rangle = \frac{1}{2}\left(T^+ + T^-\right) \tag{59}$$

$$[[T]] = T^+ - T^- \tag{60}$$

$$[[v]] = v^+ - v^- \tag{61}$$

The stability parameter used in this work is similar to the definition proposed by Dolbow and Harari[37]

$$\sigma_T \geq 8\left(\frac{A^-\|\tilde{\boldsymbol{k}}^- \cdot \hat{\boldsymbol{n}}^-\|}{V^-} + \frac{A^+\|\tilde{\boldsymbol{k}}^+ \cdot \hat{\boldsymbol{n}}^+\|}{V^+}\right) \tag{62}$$

where the only difference is the consideration of the face area of each side of the interface, where these areas are not necessarily equal. However, the definition and sensitivity of this term is still being investigated. From Eqn. VII.B.1, the finite-element discretization follows.

VII.B.2. Gas Flow at Contact Interfaces

Modeling the gas flow at contact interfaces was done through extension of Dolbow's and Harari's[37] model. To accommodate this new method, it requires modification to the governing equations' weak statements in Eqns. 5 and 6 to include additional terms due to the embedded interface. Since there are gas convection terms in both equations, each must be modified. First, if Darcy's law is assumed to define the gas velocity, the energy equation weak statement is modified to give

$$\begin{aligned}\int_\Omega \left[v\frac{\partial(\rho e_o)}{\partial t} + \boldsymbol{\nabla} v \cdot \left(\tilde{\boldsymbol{k}}\boldsymbol{\nabla} T\right) - \boldsymbol{\nabla} v \cdot \left(\phi \rho_g h_{o_g} \boldsymbol{v}_g\right) - v\boldsymbol{v}_m \cdot \boldsymbol{\nabla}(\rho e_o) - v\dot{Q}\right] d\Omega \\ + \oint_\Gamma \left(v h_{o_g}\dot{m}_g + v\dot{q}_{cond_s}\right) d\Gamma - \oint_S [[v]] \left\langle \rho_g h_{o_g} \frac{\tilde{\boldsymbol{\kappa}}}{\mu}\boldsymbol{\nabla} P \cdot \hat{\boldsymbol{n}}\right\rangle dS \\ - \oint_S \left\langle \rho_g h_{o_g} \frac{\tilde{\boldsymbol{\kappa}}}{\mu}\boldsymbol{\nabla} v \cdot \hat{\boldsymbol{n}}\right\rangle [[P]]\, dS + \oint_S \sigma_{P1}\, [[v]]\, [[P]]\, dS = 0 \quad \forall v \in H_0^1\end{aligned} \tag{63}$$

where the interface operators are defined as

$$\langle P \rangle = \frac{1}{2}\left(P^+ + P^-\right) \tag{64}$$

$$[[P]] = P^+ - P^- \tag{65}$$

Similarly, the gas continuity weak statement is rewritten as

$$\begin{aligned}\int_\Omega \left(\frac{\partial(\phi\rho_g)}{\partial t} v - \boldsymbol{\nabla} v \cdot (\phi \rho_g \boldsymbol{v}_g) - v\boldsymbol{v}_m \cdot \boldsymbol{\nabla}(\phi\rho_g) + \dot{\omega}_s v\right) d\Omega \\ + \oint_\Gamma v\dot{m}_g d\Gamma - \oint_S [[v]] \left\langle \rho_g \frac{\tilde{\boldsymbol{\kappa}}}{\mu}\boldsymbol{\nabla} P \cdot \hat{\boldsymbol{n}}\right\rangle dS \\ - \oint_S \left\langle \rho_g \frac{\tilde{\boldsymbol{\kappa}}}{\mu}\boldsymbol{\nabla} v \cdot \hat{\boldsymbol{n}}\right\rangle [[P]]\, dS + \oint_S \sigma_{P2}\, [[v]]\, [[P]]\, dS = 0 \quad \forall v \in H_0^1\end{aligned} \tag{66}$$

The stability parameter used in this work follows very closely that proposed by Dolbow and Harari.[37] For the energy equation, the stability term is determined as follows

$$\sigma_{P1} \geq 8\left(\frac{A^-\gamma_{P1}^-}{V^-} + \frac{A^+\gamma_{P1}+}{V^+}\right) \tag{67}$$

$$\gamma_{P1}^\pm = \rho_g^\pm h_{o_g}^\pm \frac{\|\tilde{\boldsymbol{\kappa}}^\pm \cdot \hat{\boldsymbol{n}}^\pm\|}{\mu^\pm} \tag{68}$$

Similarly, the stability parameter for the gas continuity equation contribution is given by

$$\sigma_{P2} \geq 8\left(\frac{A^-\gamma_{P2}^-}{V^-} + \frac{A^+\gamma_{P2}+}{V^+}\right) \tag{69}$$

$$\gamma_{P2}^\pm = \rho_g^\pm \frac{\|\tilde{\boldsymbol{\kappa}}^\pm \cdot \hat{\boldsymbol{n}}^\pm\|}{\mu^\pm} \tag{70}$$

From Eqns. VII.B.2 and VII.B.2, the finite-element discretization follows.

VIII. Example Thermochemical Ablation Problem: PICA Iso-Q in Arcjet

Consider a $4\,\mathrm{inch}$ diameter iso-q attached to a cylindrical base, which is characteristic of arcjet test specimens used for thermal protection material testing. The iso-q is made of Phenolic Impregnated Carbon Ablator (PICA), and the cylindrical base is made of LI-2200, which is a silica based insulating material. The schematic of the test specimen can be seen in Figure 6, which includes both dimensions and material split lines. The figure shows one plane of the axisymmetric body. Also, the test specimens were constructed in a piece-wise manner as discussed by Agrawal,[39] but no bonding agent was used to join the components. This specimen design lends itself to be easily modeled since no adhesive layers need to be included. For the current calculation, the PICA sections are assumed to be in perfect contact so no contact resistance model is included. Several samples with different thermocouple (TC) locations were tested consecutively at identical conditions. Consequently, the data and comparisons presented here are a conglomeration of three different sample exposures all tested at the same condition.

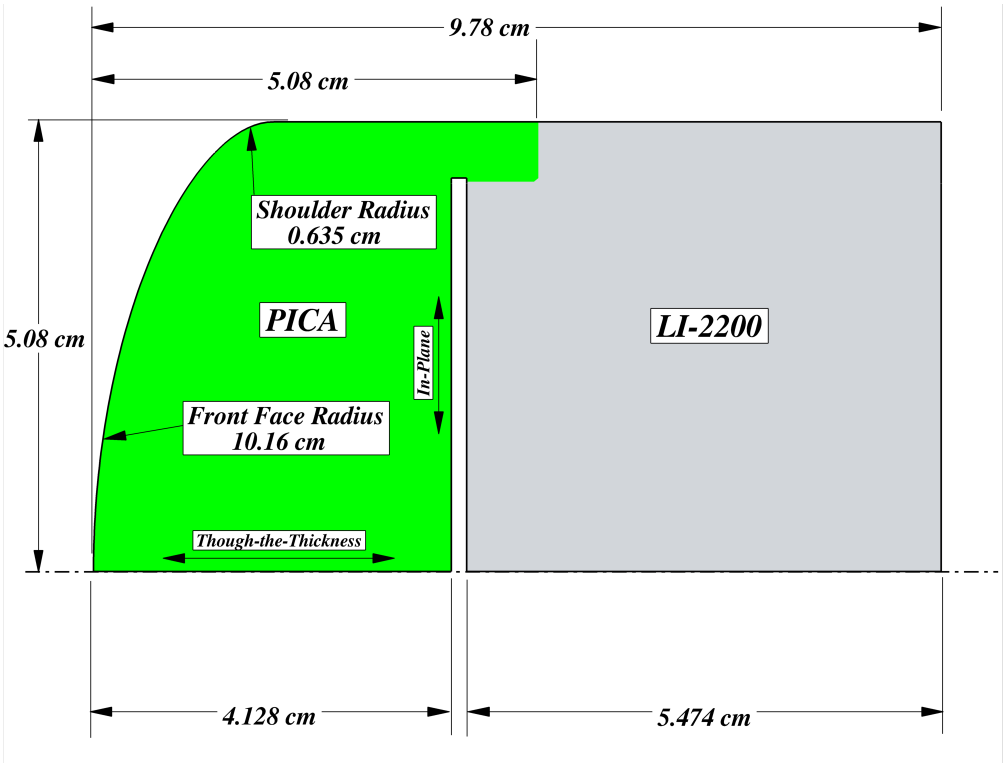

Figure 6. PICA problem iso-q geometry.

The material model inputs for both PICA and LI-2200 are not included in this document due to publication restrictions. However, there is limited permeability information for PICA available in the open literature,[29] and those values are used here. A second permeability model was derived in an attempt to make *CHAR* mimic the physical modeling assumptions in legacy ablation codes. Consequently, the virgin permeability was minimized, and the char permeability was maximized such that a stable solution could be reached. This effectively forces all of the pyrolysis gas generated in-depth to be pushed to the surface as quickly as possible. However, it should be noted that it is not possible for *CHAR* to be altered to employ all of the same physical modeling assumptions of the legacy tools.

While the TC traces suggest a wide variability in initial temperature, for the *CHAR* simulation the specimen is initially at $294.25\,\mathrm{K}$. The initial pressure condition is not known, but it should be low since the test chamber is evacuated prior to a run. For the *CHAR* simulation, the pressure was initialized to $800\,\mathrm{Pa}$, which is an order of magnitude less than the surface pressure at the stagnation point ($8581\,\mathrm{Pa}$). A study was performed to assess the sensitivity of the solution to the initial pressure condition. It was found that the initial pressure made little difference to the solution as long as it was an order of magnitude or more lower than the stagnation pressure.

The PICA is exposed to a convective heating boundary condition shown in Figure 7 for $42\,\mathrm{sec}$ and allowed to reradiate to $340\,\mathrm{K}$. The recovery enthalpy is assumed to be constant across the surface at the freestream total value, $h_r = 19.0\,\mathrm{MJ/kg}$ for a $298\,\mathrm{K}$ reference temperature. This is a good assumption in the stagnation region, but it is

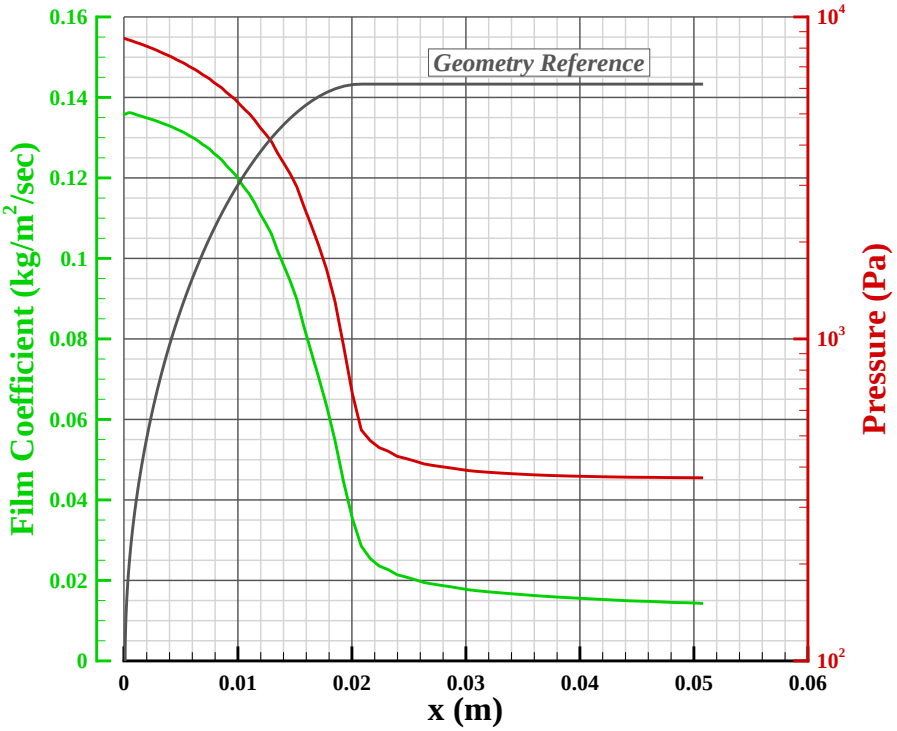

Figure 7. PICA problem film coefficient and surface pressure conditions.

erroneously high in the sidewall region. The convective heating and pressure conditions were derived using a computational fluid dynamics simulation from the DPLR CFD code.[40] The flow was assumed to be laminar, and the blowing reduction parameter (λ) was set to 0.5. The arcjet stream is partially dissociated air with argon, and the surface thermochemistry tables appropriately account for the environment gases reactions with PICA. The LI-2200 on the sides of the cylinder is assumed to be exposed to a constant heat flux of $25\,{}^{\mathrm{W}}/_{\mathrm{cm}^2}$ during the $42\,\mathrm{sec}$ exposure, and it also reradiates to $340\,\mathrm{K}$. The base of the LI-2200 is assumed to be adiabatic throughout the simulation. The surfaces surrounding the gap between the PICA and LI-2200 are assumed to be adiabatic since the enclosure radiation exchange is minimal at the temperature differences the two sides will see. The PICA boundaries around this gap are assumed to be impermeable. This is likely true only if the PICA was coated with an adhesive or sealant, but those details about the specimen construction are not known. Pyrolysis gases are not allowed to flow into the LI-2200.

After the $42\,\mathrm{sec}$ exposure, the model experiences a $538\,\mathrm{sec}$ cool-down during which it reradiates to $340\,\mathrm{K}$. During the cool-down phase, the PICA is still allowed to pyrolyze, and pyrolysis gas rejection from the surface is still accounted for in the surface boundary condition. The surface pressure condition is reduced by an order of magnitude relative to what is shown in Figure 7 since removal from the arcjet stream would put the specimen back into its initial low pressure state. While data was taken for the entire $600\,\mathrm{sec}$, the first $100\,\mathrm{sec}$ ($42\,\mathrm{sec}$ exposure plus a $58\,\mathrm{sec}$ cool down) will be looked at in detail.

The data presented is a conglomeration of three test specimens at the same conditions. The heating environments for all three tests are the same within the facility's ability to repeat and/or maintain a condition. One specimen was instrumented with five TCs on the center axis. The second and third specimens had nine TCs. Three TCs were on the center axis, and six TCs were off-axis. Both specimens had the same TC locations to give repeat data. Altogether, there were 10 unique TC locations as shown in Table 2 with most locations having redundant data as denoted in the table. Notice that the total number of TCs represented in Table 2 is 22, and the total number of TCs in the specimens is 23. This is because the final data available to the authors was missing one TC trace at the TC 2 location. All the TCs are in PICA, which can be seen in Figure 8. The uncertainty in the reported temperature is not known, therefore no error bars are reported with the data traces.

The problem was run with several different assumptions which are outlined in Table 3. The surface boundary condition for the one-dimensional simulation, case 1, was assumed to be the same as the stagnation point conditions

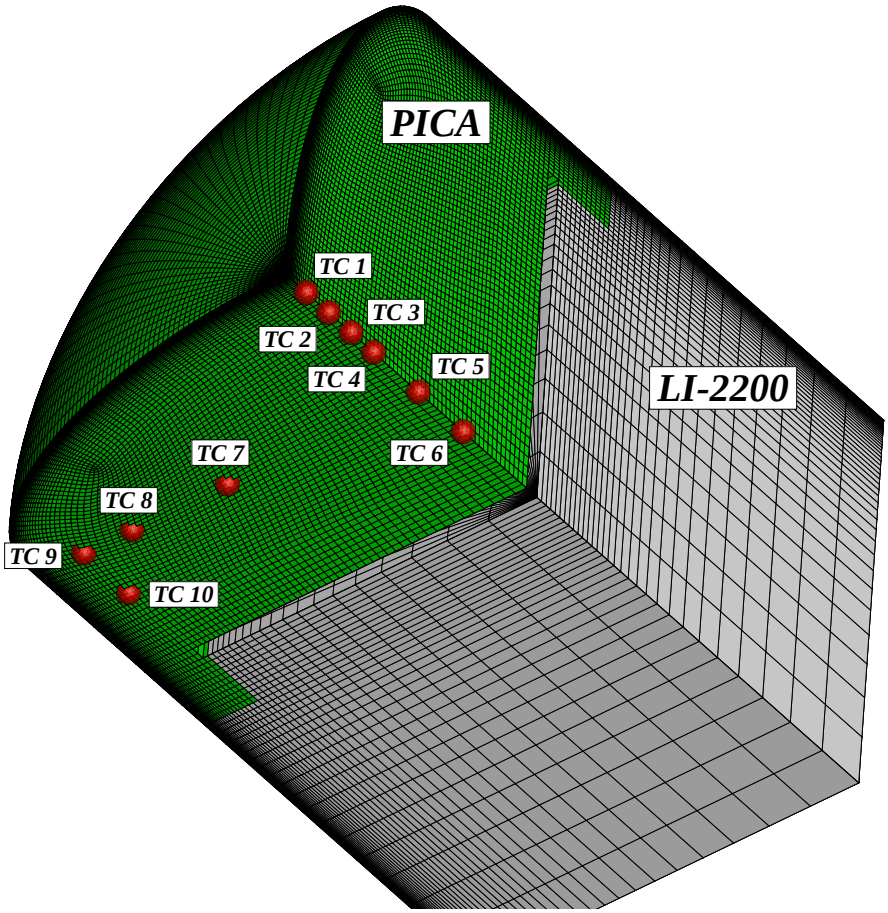

Figure 8. PICA problem three-dimensional grid and thermocouple locations.

Table 2. PICA problem thermocouple locations.

Name	Depth (cm)	Radius (cm)	Redundancy
TC1	0.381	0.0	1
TC2	0.762	0.0	2
TC3	1.143	0.0	1
TC4	1.524	0.0	1
TC5	2.286	0.0	2
TC6	3.048	0.0	3
TC7	2.286	2.54	2
TC8	2.286	3.81	2
TC9	2.286	4.45	2
TC10	3.048	4.45	6

Table 3. PICA problem case matrix.

Case	Dimensions	Permeability Model
1	1D	A
2	2D Axi	A
3	2D Axi	B
4	3D	A

Table 4. PICA permeability models.

	Model A				Model B [29]			
	Through-the-Thickness		In-Plane		Through-the-Thickness		In-Plane	
β	κ_o, m^2	b, Pa	κ_o, m^2	b, Pa	κ_o, m^2	b, Pa	κ_o, m^2	b, Pa
0	1.0e-12	0	1.0e-12	0	13.3e-12	3.85e3	34.9e-12	2.09e3
1	1.0e-10	0	1.0e-10	0	38.1e-12	2.5e3	53.8e-12	1.87e3

for the multi-dimensional cases.

The permeability models are given in Table 4. Permeability model A was chosen so that all of the pyrolysis gases would be pushed toward the surface while minimizing the flow through virgin PICA. The through-the-thickness and in-plane models are assumed to be the same so there is no preferential direction for the gas to flow. Although this model was chosen to make *CHAR* behave like legacy codes, lateral gas flow with respect to the surface cannot be completely eliminated since there is a strong pressure gradient across the heated surface as shown in Figure 7. Permeability model B was taken from a study done by Marschall.[29]

All four cases were run with the same time step scheme shown in Table 5, and the time step was assumed to vary linearly between entries. The one-dimensional grid had 200 elements with a constant stretching ratio of 1.05. The two-dimensional grid, which is comprised entirely of quadrilateral elements, can be seen in Figure 9. The three-dimensional grid, which is made of all hexahedral elements with the exception of the prisms on the axis, can be seen in Figure 8. The three-dimensional grid took advantage of symmetry to reduce computational time. The temperature solutions were all shown to be spatially and temporally grid converged.

Table 5. PICA problem time step schedule.

Time (sec)	Time Step (sec)
0.0	0.005
2.0	0.25
42.0	0.25
50.0	0.5
100.0	0.5

VIII.A. Numerical Results with Test Data

For all of the comparisons with test data, the *CHAR* solution from case 2 in Table 3 was used. It is important to point out that the TC measurement and junction location uncertainties are not accounted for in the comparisons. Additionally, the TC wires were not modeled in the simulation, and no contact resistance or thermal lag models were used in the comparisons.

A comparison with centerline TCs 1, 2, 3, and 4 can be seen in Figure 10. During the heat pulse ($0 - 42\,\mathrm{sec}$), *CHAR*'s agreement with the data is reasonable with the *CHAR* prediction being higher than the data except at early times. The data for TC 1 stops around $27\,\mathrm{sec}$ because the TC has reached its calibration limit and starts to provide poor data. For TC 2, the redundant measurements do not agree very well. While it can not be said for certain, it appears that the lower trace may be from a faulty TC given that it is an outlier from the rest of the data set, and the trace

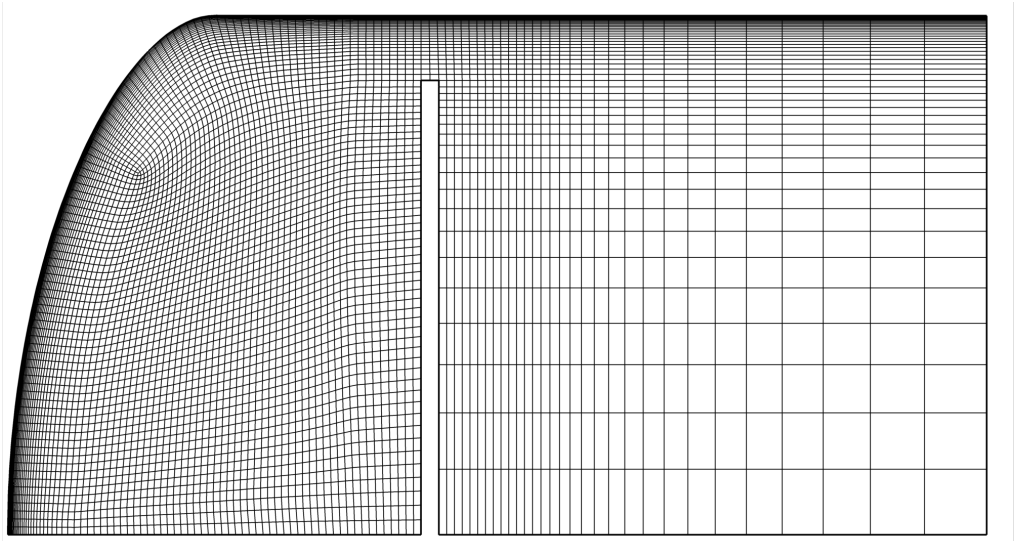

Figure 9. PICA problem two-dimensional grid.

has significantly more noise than all the other TC traces. After the heat pulse, the *CHAR* results show a more rapid cool-down than the data suggests. This could either be due to deficiencies in the model or poorly defined boundary conditions during that phase of the test.

A comparison with TCs 5, 7, 8, and 9, which are all $2.286\,\mathrm{cm}$ deep, can be seen in Figure 11. Again, the agreement is reasonable during the heat pulse but begins to worsen during the cool-down phase. It is evident from Figure 11 that not all TCs were reporting the same temperature at time zero. Also, there is significant variability in the redundant data. This could be due to condition variability, model fabrication differences, and variability in thermal properties between samples. It is possible that there was an anomaly for the TC 9 trace that was initially near $400\,\mathrm{K}$. Neither the starting temperature nor the trend seem to be consistent with the rest of the data set.

A comparison with TCs 6 and 10, which are both $3.048\,\mathrm{cm}$ deep, can be seen in Figure 12. There is a wide variation for the TC 10 data, including in the initial conditions, but the agreement is again reasonable. It is evident from the TC 6 traces that there is an early temperature rise and plateau between 20 and 40 seconds that is not captured in the model. This phenomenon has been seen in many PICA arcjet tests and is thought to be due to water phase change, which is not being modeled in *CHAR*.

The measured surface recession at the centerline was $0.406\,\mathrm{cm}$. It is not clear if this is taken from one specimen or is an average of the three specimens. Also, the uncertainty on this measurement is not known. *CHAR* predicted a centerline recession of $0.378\,\mathrm{cm}$ which is a 7% under-prediction.

Overall, the agreement with the data is reasonable but there is certainly room for improvement for the *CHAR* PICA model. Given the assumptions that went into developing the boundary conditions and the wide variation in the redundant TC data, the comparison is satisfactory, but it is recognized that forward work must be done to investigate the validity of the PICA model for use in *CHAR* over a wider range of environmental conditions.

VIII.B. Dimensionality Effects

For cases 1, 2, and 4, where the only difference is the dimensionality of the problem, a comparison for centerline TCs 1-6 can be seen in Figure 13. Only the centerline TCs can be examined for this comparison since the one-dimensional case cannot model the off-centerline TCs. The two- and three-dimensional solutions are coincident at all TC locations, including those not shown in the plot. This is the expected result since the problem is axisymmetric and both cases are grid converged. This confirms that the implementation of the axisymmetric and anisotropic conduction terms are consistent between the two options in the code.

For the surface and all TC locations, the one-dimensional solution shows lower temperatures. Since the one-dimensional assumption assumes an infinite planar slab in all directions, there is significantly more thermal mass to absorb energy from the environment thereby decreasing the heat getting to the centerline TCs. Also since the one-dimensional case only simulates the stagnation point, all of the pyrolysis gases getting to the surface are going through the stagnation point. This will maximize the blowing reduction effects thereby decreasing the stagnation point heat

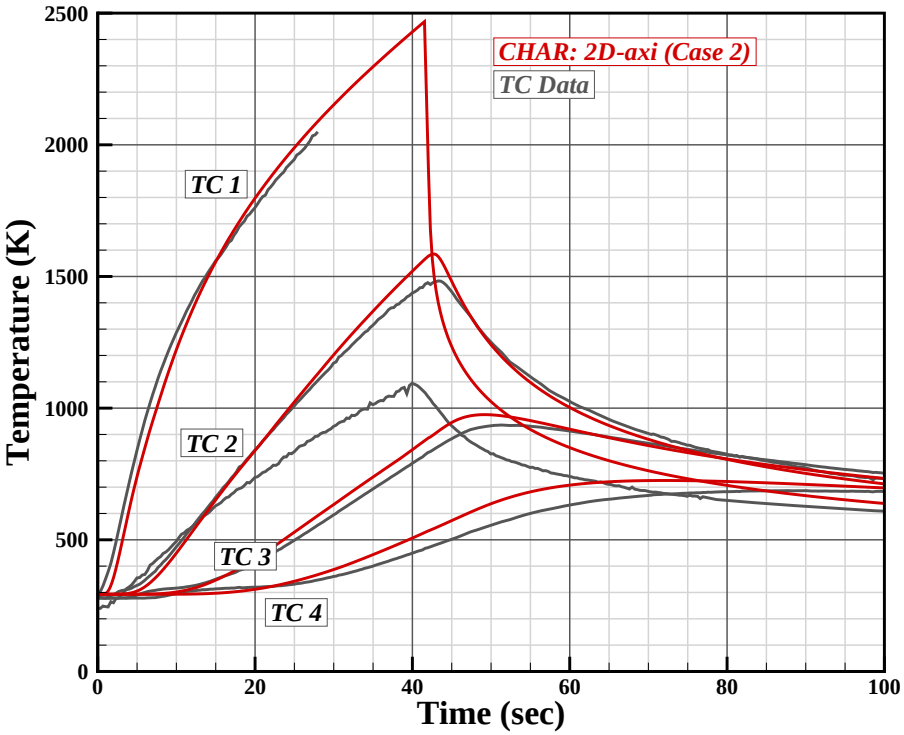

Figure 10. Code-to-data comparison for TCs 1, 2, 3, and 4.

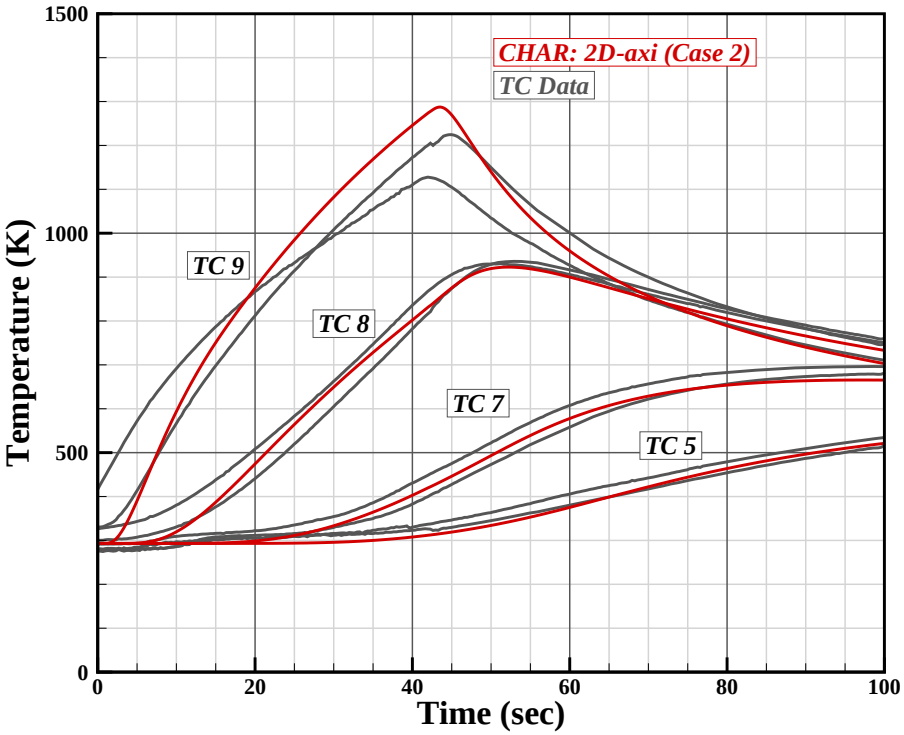

Figure 11. Code-to-data comparison for TCs 5, 7, 8, and 9.

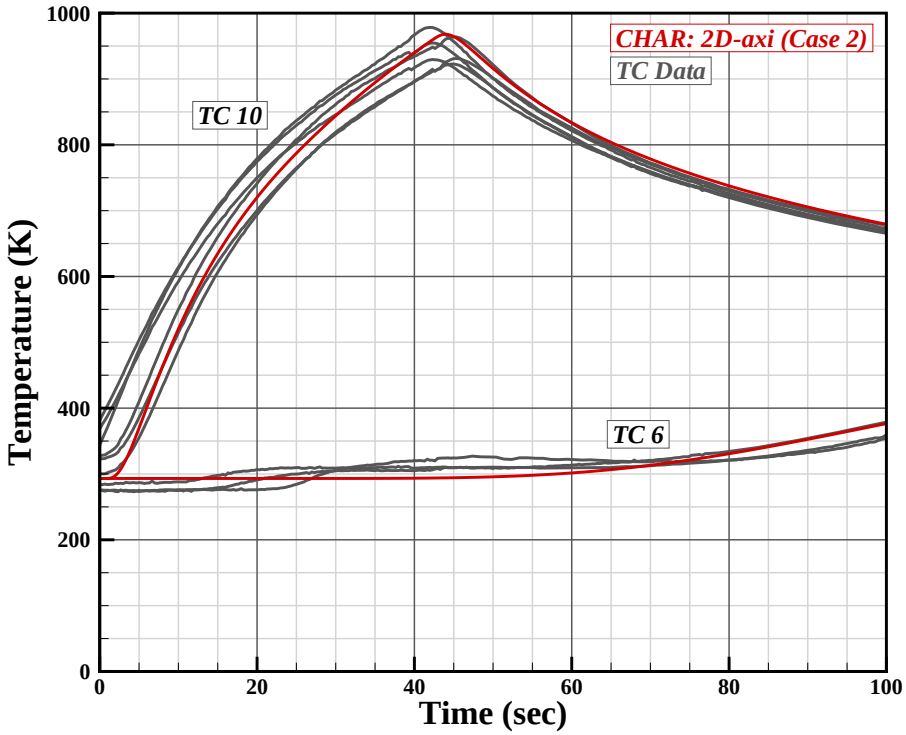

Figure 12. Code-to-data comparison for TCs 6 and 10.

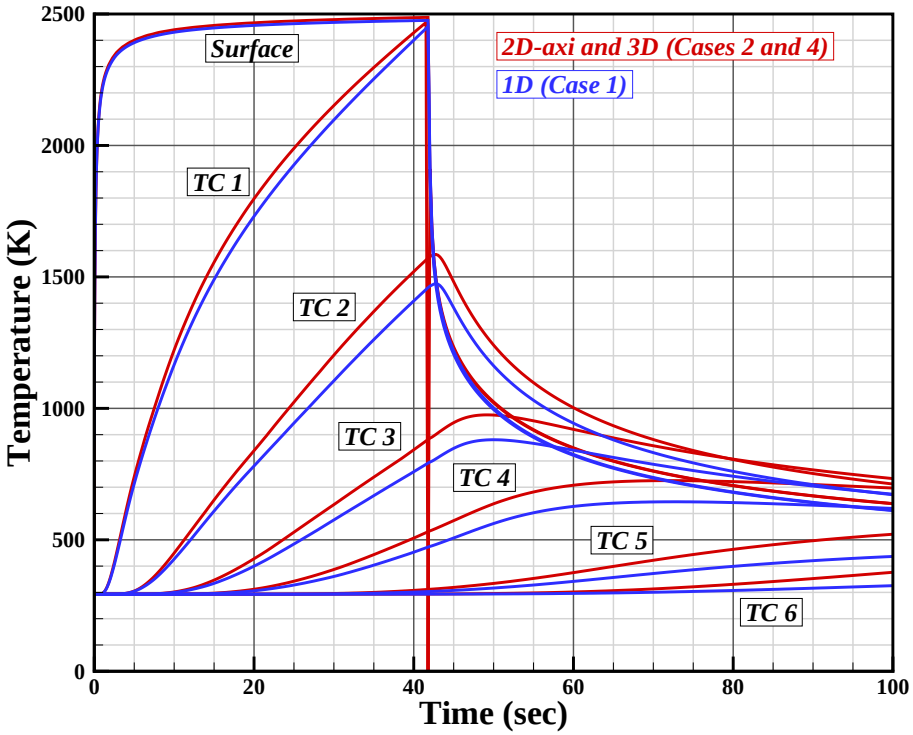

Figure 13. One-, two-, and three-dimensional *CHAR* results for centerline TCs 1-6.

flux more than is seen in the multi-dimensional cases.

VIII.C. Permeability Modeling

A comparison of permeability models A and B in cases 2 and 3 respectively can be seen in Figures 14-16. Permeability model B over-predicts the temperature results for model A at all TC locations except TCs 9 and 10, which are the two TCs closest to the specimen sidewall. One difference between the permeability models is that model B is anisotropic with a higher permeability in the in-plane direction than in the through-the-thickness direction. Therefore the preferential direction for the pyrolysis gases to flow for model B is out the sidewall, which is also promoted by the low sidewall pressure. Consequently, the blowing reduction in the stagnation region is much more significant for model A resulting in lower stagnation point heat fluxes and lower in-depth temperatures relative to model B. The opposite is true on the sidewall where model B will have a more significant blowing reduction.

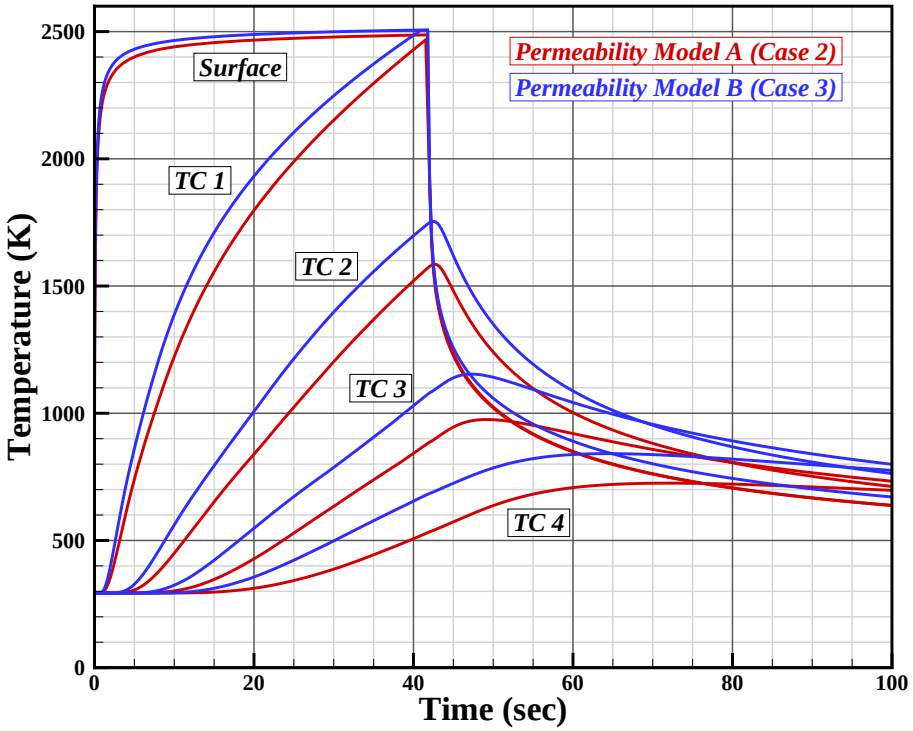

Figure 14. Permeability model comparison for TCs 1, 2, 3, and 4.

The pyrolysis gas mass flux solutions at $40\,\mathrm{sec}$ are shown in Figure 17. The mass flux direction is denoted by the streamlines, and the magnitude is denoted by the contour level. The pink lines denote where the degree of char, β, is between 0.02 and 0.98, which is a common way to define the pyrolysis zone. While the mass flow directions are similar between the two models, it is evident that model A is focusing the bulk of the mass flow toward the surface while not letting gas flow through the relatively impermeable virgin layer. For model B on the other hand, much of the pyrolysis gas generated in the stagnation region is free to flow into the virgin material and eventually flows out the sidewall. Consequently, the two models will predict different blowing reductions across the heated surface which is a major contributor to the differences in the temperature field.

It is evident from this exercise that it is necessary to develop a PICA response model that is consistent with the physical modeling assumptions in *CHAR*. Using a fabricated permeability model to mimic legacy code behavior may provide a reasonable temperature solution, but the pressure and mass flux fields may be grossly mis-predicted. Dedicated tests with both temperature and pressure instrumentation would be required to provide model development and validation data for *CHAR*.

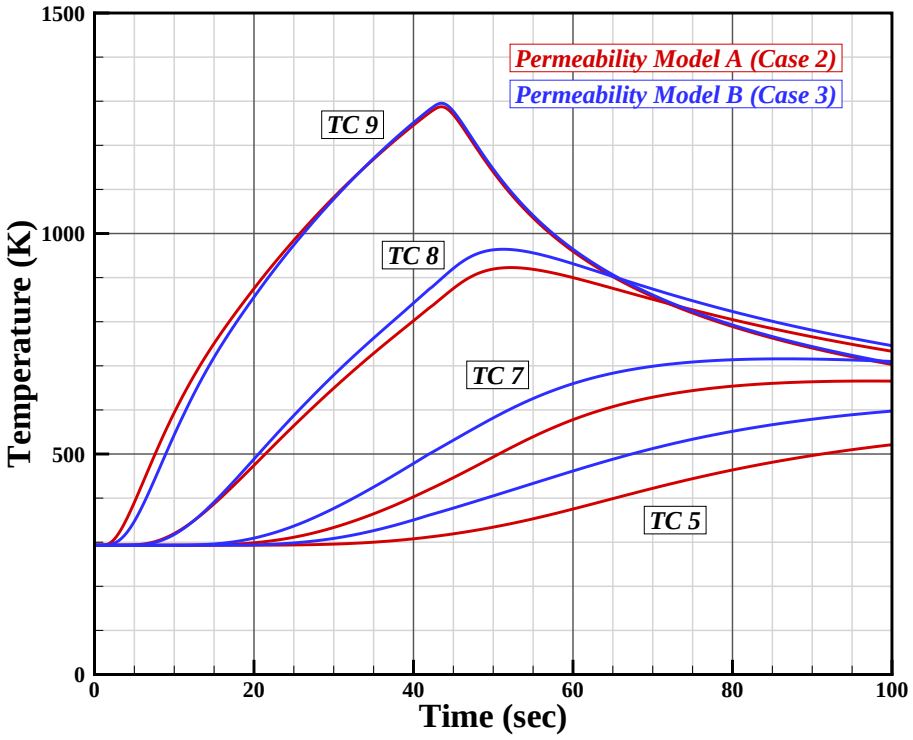

Figure 15. Permeability model comparison for TCs 5, 7, 8, 9.

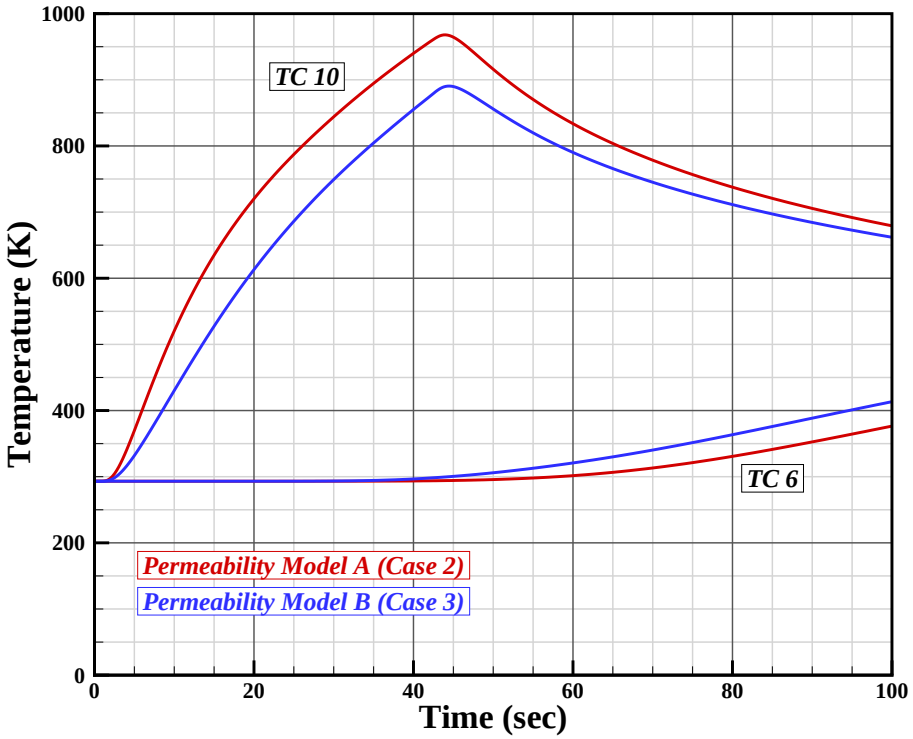

Figure 16. Permeability model comparison for TCs 6 and 10.

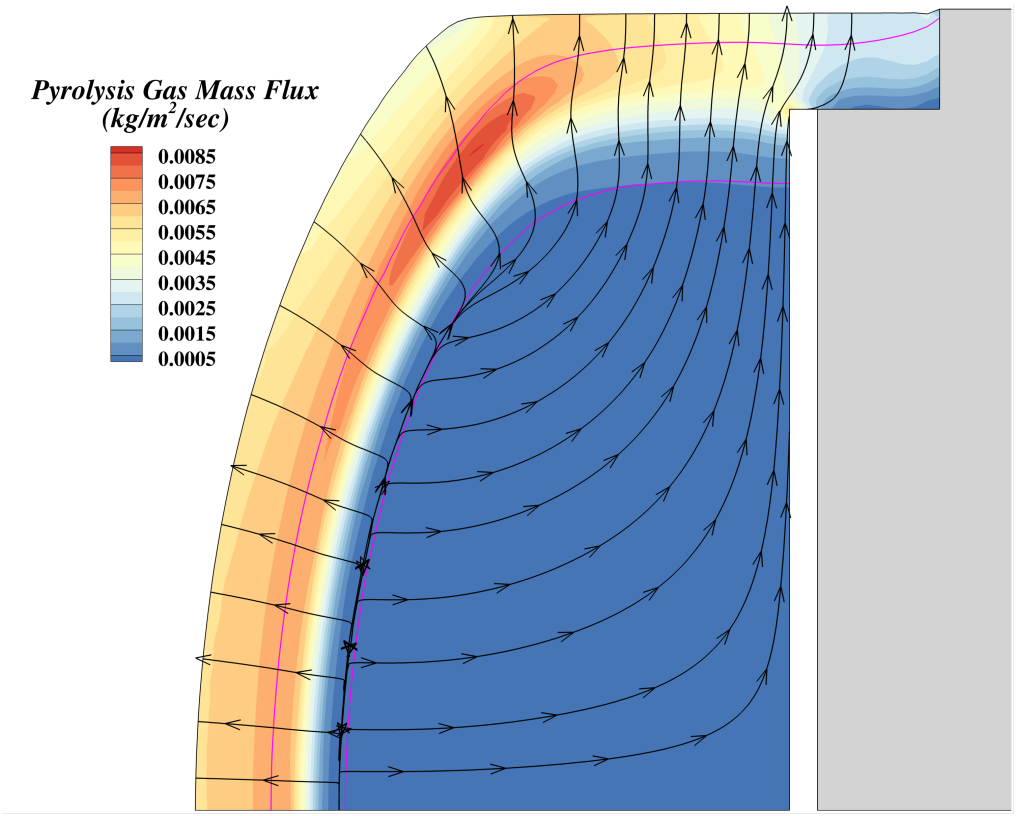

(a) Permeability model A

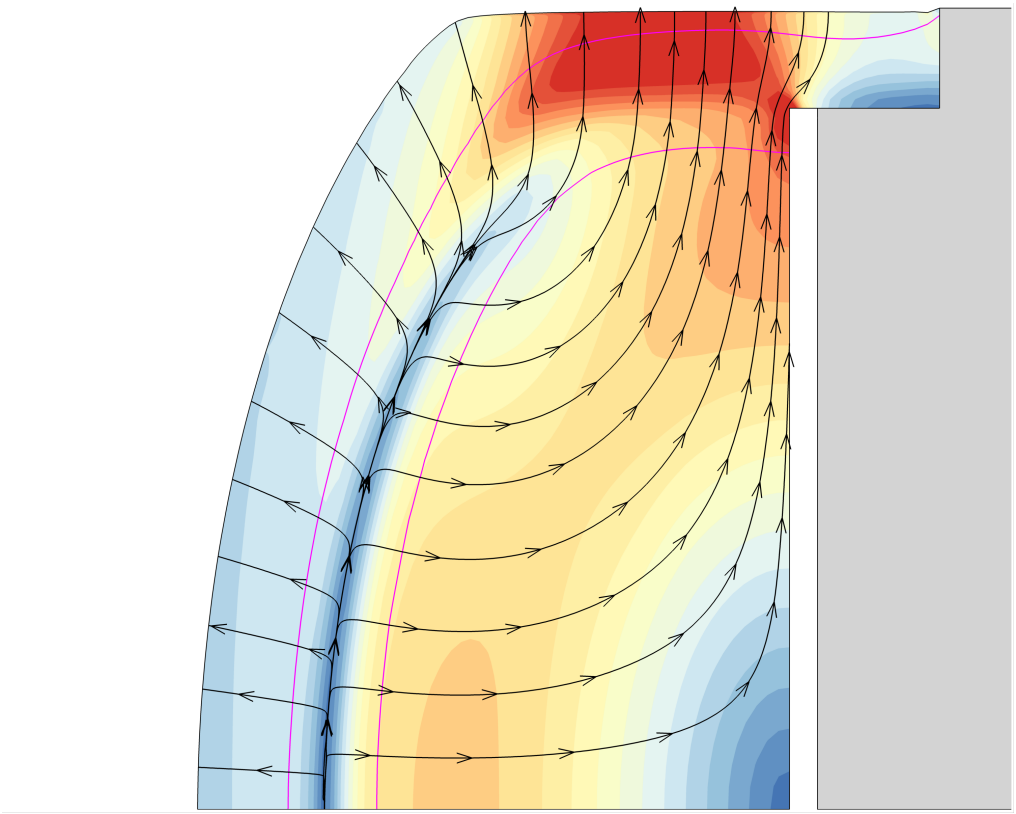

(b) Permeability model B

Figure 17. Mass flux solutions at 40 sec (pyrolysis zone, $\beta = 0.02$ and 0.98, highlighted in pink).

VIII.D. With Contact Surfaces and Adaptive Mesh Refinement

In an attempt to demonstrate other functionality, case 2 will be repeated with the addition of contact interfaces embedded in the mesh and adaptive mesh refinement (AMR). The contact interface modeling has been described in Section VII.B, and the AMR functionality in *CHAR* is supplied by `libMesh`. Algorithm details and other applications are provided by Kirk.[26] The AMR implementation in *CHAR* allows the user to refine and coarsen elements based on error estimates or solution features. For this problem, feature based refinement was used. Elements would be refined if β on any node was between ? and ?, and they would be candidates for coarsening if β on all nodes was not between ? and ?. Elements were limited to one refinement, which implies that no element face would have more than two elements as neighbors. AMR was allowed every ? timesteps, and only once within a given timestep. Within a timestep, the logic flow is:

Iteratively converge nonlinear system $\rightarrow$ Refine Mesh $\rightarrow$ Iteratively converge nonlinear system on new mesh

The initial mesh for the problem can be seen in Figure 18a. Notice that there is a region of triangle elements that are not aligned, node-for-node, with the surrounding quadrilateral mesh. Other than this section of triangle elements, the mesh is identical to the case 2 quadrilateral mesh in Figure 9. The interface of the triangle and quadrilateral meshes are modeled with perfect thermal and gas flow contact conditions. As mentioned in Section VII.B, there is a restriction in *CHAR* such that the mesh motion DoFs on a contact boundary cannot depend on the mesh motion DoFs across the contact boundary. Therefore, the contact boundaries must remain fixed during the solution process although the material is ablating.

The thermocouple traces shown in Figure 19 indicate that the presence of the contact interfaces did not impact the temperature field solution. While this does not verify the implementation, it does improve confidence in the capability. Additionally, Figure 20 shows temperature (colors) and pressure (lines) contours at $50\,\mathrm{sec}$, which indicate smooth contour lines in both field variables across the interface boundaries. Figure 18 shows the progression of mesh recession and adaptive mesh refinement throughout the solution. Figure 18c indicates that refinement occurred in both quadrilateral and triangle elements. A closer look at the final mesh in the interface region can be seen in Figure 21 where the $\beta = 0.02$ and 0.98 contours are highlighted in white. It is evident that the adapted region is contained between these two contours as expected.

IX. Thermoelastic Solver

CHAR has the ability to solve the linear thermoelastic equations in a one-way coupled quasi-steady fashion to give the displacement, stress, and strain fields for a body under thermoelastic loading. The equations are linearized by only considering the linear terms in the strain-displacement relationships and by assuming that the material properties are not functions of the displacement. The thermoelastic equations are one-way coupled to the thermal and ablation equations such that an instantaneous temperature field provided from the thermal and ablation solver is assumed to be fixed during the thermoelastic solve. There is no feedback from the thermoelastic solver to the energy equation either in the form of solid deformation or thermoelastic coupling terms in the energy equation. The thermoelastic solver can be thought of as a post-processing of the thermal and ablation equations that can occur at a user-defined frequency. In the current implementation, the pressure field within a decomposing ablator is not considered to contribute to the thermoelastic response. It is recognized that this capability must be added to predict internal pressure induced spallation or delamination.

The solution to the thermoelastic equations is quasi-steady in that the displacement field, $\boldsymbol{u}$, is assumed to be static at the end of each solve. This implies that

$$\frac{\partial \boldsymbol{u}}{\partial t} = \boldsymbol{0} \tag{71}$$

The physical assumption is that the material elastically responds quickly relative to changes in the temperature field.

IX.A. Governing Equations

The equations that govern the steady thermoelastic response of a solid under loading are

$$\boldsymbol{\nabla} \cdot \tilde{\boldsymbol{\sigma}} + \boldsymbol{f} = \boldsymbol{0} \tag{72}$$

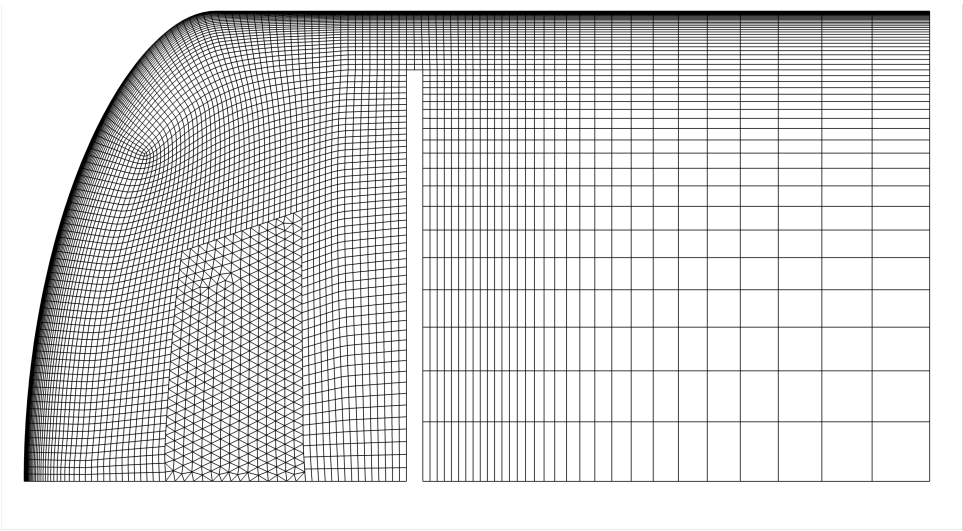

(a) Initial Mesh (0 sec)

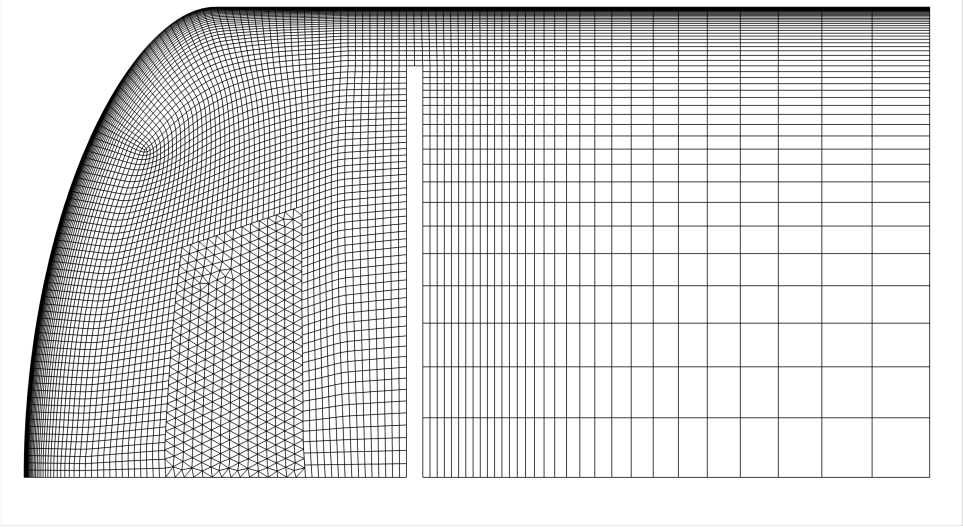

(b) Intermediate Mesh (20 sec)

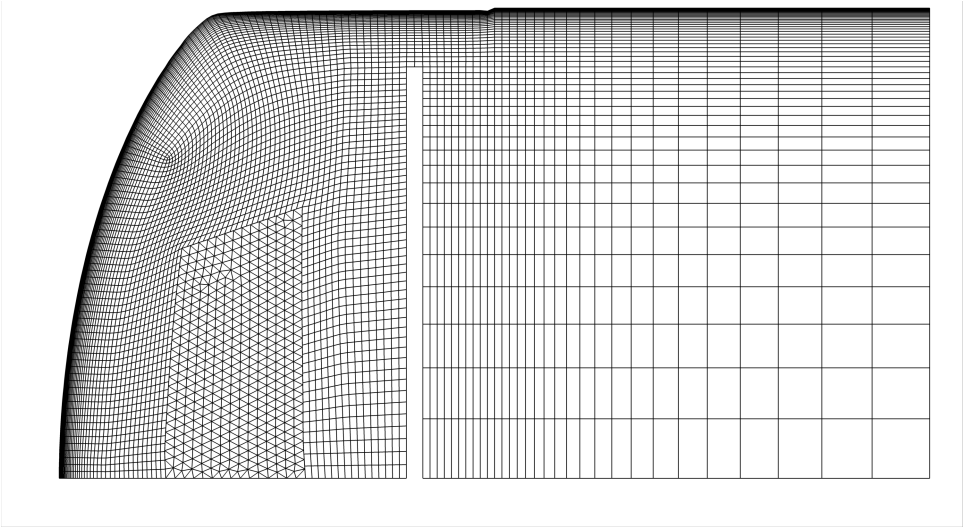

(c) Final Mesh (100 sec)

Figure 18. Initial and final AMR mesh with contact surfaces.

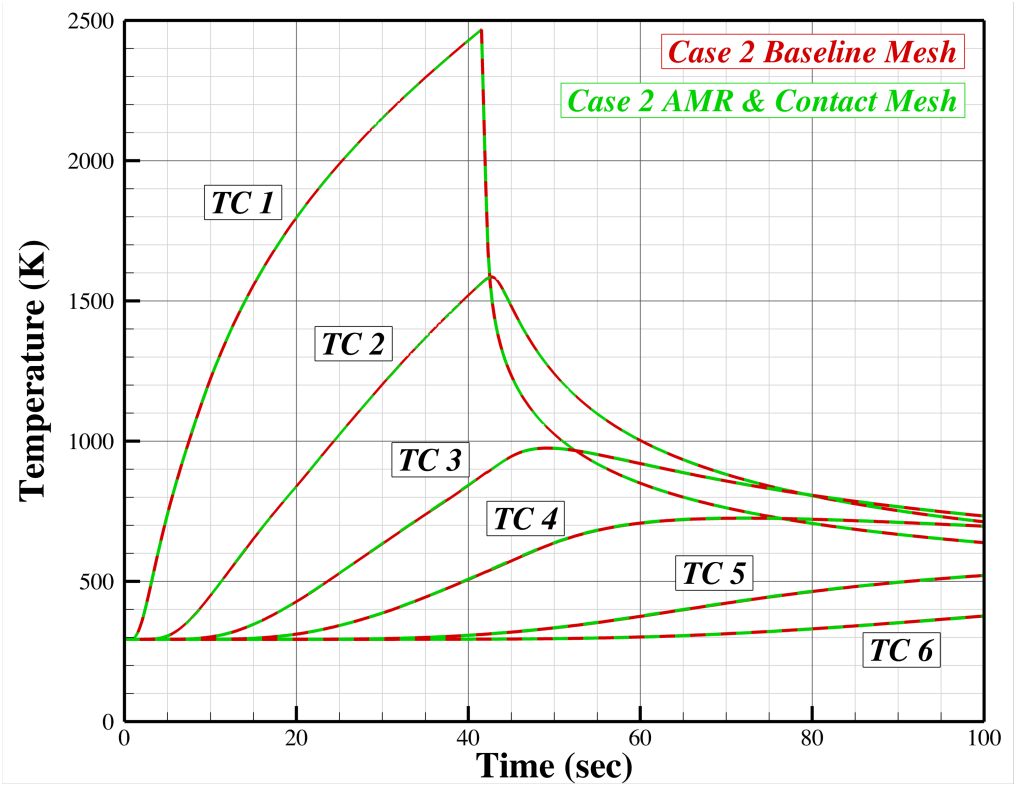

Figure 19. Case 2 temperature traces from baseline mesh and AMR mesh with contact interfaces.

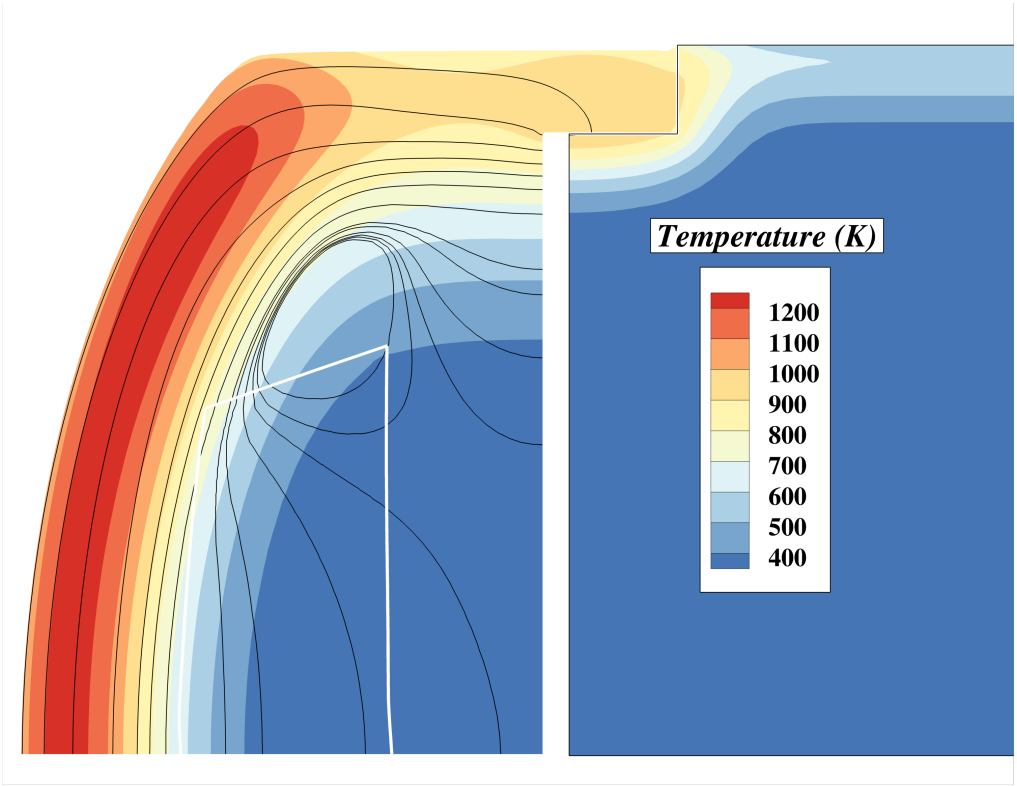

Figure 20. Temperature (colors) and pressure (lines) at 50 sec (contact interface highlighted in white).

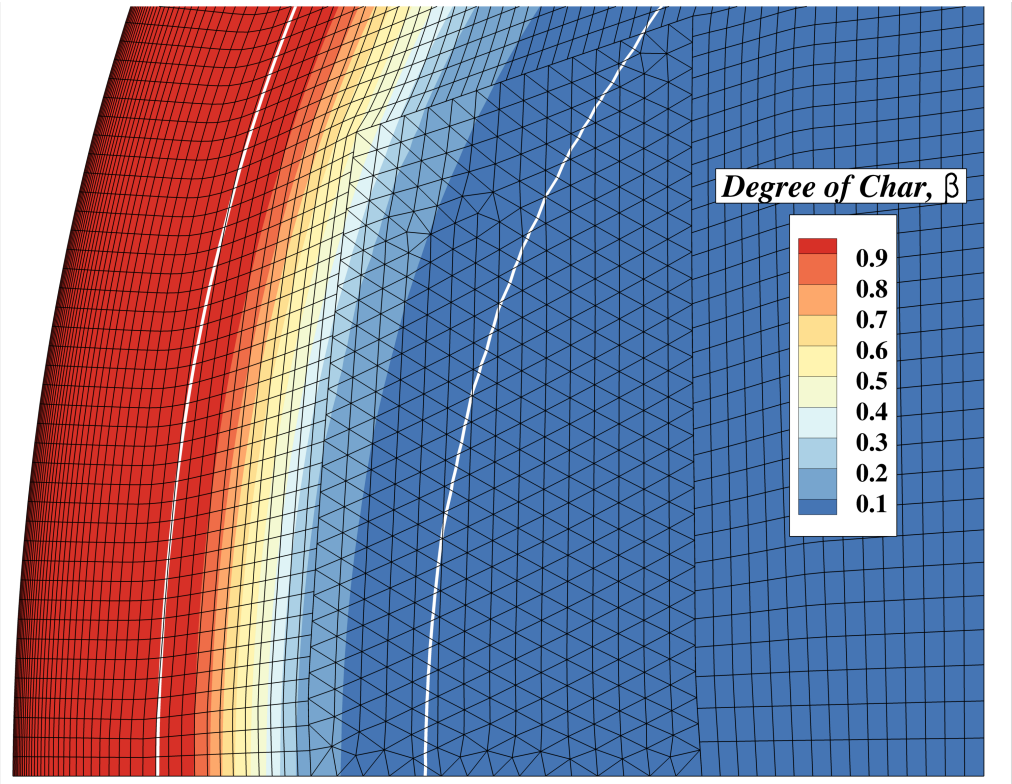

Figure 21. Degree of char contours on final mesh 100 sec ($\beta = 0.02$ and 0.98 highlighted in white).

where $\tilde{\boldsymbol{\sigma}}$ is the stress tensor, $\boldsymbol{f}$ is the body force per unit volume, and $\boldsymbol{u}$ is the unknown displacement field, which is embedded in the definition of the stress tensor.

$$\boldsymbol{u} = \begin{bmatrix} u_1 \\ u_2 \\ u_3 \end{bmatrix} \tag{73}$$

The symmetric stress tensor is defined as

$$\tilde{\boldsymbol{\sigma}} = \begin{bmatrix} \sigma_{11} & \sigma_{12} & \sigma_{13} \\ \cdot & \sigma_{22} & \sigma_{23} \\ \cdot & \cdot & \sigma_{33} \end{bmatrix} = \begin{bmatrix} \boldsymbol{\sigma}_1 & \boldsymbol{\sigma}_2 & \boldsymbol{\sigma}_3 \end{bmatrix} \tag{74}$$

where the diagonal terms are the normal stresses and the off-diagonal terms are the shear stresses. where

$$\boldsymbol{\sigma}_d = \begin{bmatrix} \sigma_{1d} \\ \sigma_{2d} \\ \sigma_{3d} \end{bmatrix} \quad \text{for } d = 1, 2, 3 \tag{75}$$

The linear elasticity equation for each dimension can now be written as

$$\boldsymbol{\nabla} \cdot \boldsymbol{\sigma}_d + f_d = 0 \quad \text{for } d = 1, 2, 3 \tag{76}$$

In order to derive the relationship between the stress and the displacements, it is necessary to recognize that the orthogonal 123-coordinate system that the problem is solved in (denoted as the "problem coordinate system" from here on) is in general not the same orthogonal $1'2'3'$-coordinate system that the material properties are defined in (denoted as the "material coordinate system" from here on). Any value, vector, or tensor followed by the prime symbol, '′', will be with respect to the material coordinate system, while any non-primed value, vector, or tensor will be with respect to the problem coordinate system.

In the material coordinate system, the stress is related to the strain via Hooke's law for small deformations

$$\tilde{\boldsymbol{\sigma}}' = \tilde{\boldsymbol{K}}' : \left[\tilde{\boldsymbol{\varepsilon}}' - \Delta T \tilde{\boldsymbol{\alpha}}'\right] \tag{77}$$

where the strain, $\boldsymbol{\varepsilon}'$, is also a symmetric tensor and is defined via the linear strain-displacement relationship

$$\tilde{\boldsymbol{\varepsilon}}' = \frac{1}{2}\left[\boldsymbol{\nabla u}' + (\boldsymbol{\nabla u}')^T\right] \tag{78}$$

$\Delta T \boldsymbol{\alpha}'$ are the thermal strains where

$$\tilde{\boldsymbol{\alpha}}' = \begin{bmatrix} \alpha_1' & 0 & 0 \\ \cdot & \alpha_2' & 0 \\ \cdot & \cdot & \alpha_3' \end{bmatrix} \tag{79}$$

and α_i' are the coefficients of thermal expansion. $\tilde{\boldsymbol{K}}'$ is the fourth-order stiffness tensor containing the 81 elastic coefficients, k_{ijkl}', which are properties of the material and are defined with respect to the material's coordinate system. Because of the linear assumption, the elastic coefficients are independent of the displacement, but they do vary with temperature. Due to symmetry, there are only 21 independent elastic coefficients in the stiffness tensor. Consequently, Voigt notation is often used to represent the stress and strain tensors to reduce the order of the problem.

$$\boldsymbol{\sigma}_v' = \begin{bmatrix} \sigma_{11}' \\ \sigma_{22}' \\ \sigma_{33}' \\ \sigma_{23}' \\ \sigma_{13}' \\ \sigma_{12}' \end{bmatrix}, \boldsymbol{\varepsilon}_v' = \begin{bmatrix} \varepsilon_{11}' \\ \varepsilon_{22}' \\ \varepsilon_{33}' \\ 2\varepsilon_{23}' \\ 2\varepsilon_{13}' \\ 2\varepsilon_{12}' \end{bmatrix}, \boldsymbol{\alpha}_v' = \begin{bmatrix} \alpha_1' \\ \alpha_2' \\ \alpha_3' \\ 0 \\ 0 \\ 0 \end{bmatrix} \tag{80}$$

and the stiffness tensor is simplified to

$$\tilde{\boldsymbol{K}}_v' = \begin{bmatrix} k_{1111}' & k_{1122}' & k_{1133}' & k_{1123}' & k_{1131}' & k_{1112}' \\ k_{2211}' & k_{2222}' & k_{2233}' & k_{2223}' & k_{2231}' & k_{2212}' \\ k_{3311}' & k_{3322}' & k_{3333}' & k_{3323}' & k_{3331}' & k_{3312}' \\ k_{2311}' & k_{2322}' & k_{2333}' & k_{2323}' & k_{2331}' & k_{2312}' \\ k_{3111}' & k_{3122}' & k_{3133}' & k_{3123}' & k_{3131}' & k_{3112}' \\ k_{1211}' & k_{1222}' & k_{1233}' & k_{1223}' & k_{1231}' & k_{1212}' \end{bmatrix} = \begin{bmatrix} K_{11}' & K_{12}' & K_{13}' & K_{14}' & K_{15}' & K_{16}' \\ \cdot & K_{22}' & K_{23} & K_{24} & K_{25} & K_{26} \\ \cdot & \cdot & K_{33}' & K_{34}' & K_{35}' & K_{36}' \\ \cdot & \cdot & \cdot & K_{44}' & K_{45}' & K_{46}' \\ \cdot & \cdot & \cdot & \cdot & K_{55}' & K_{56}' \\ \cdot & \cdot & \cdot & \cdot & \cdot & K_{66}' \end{bmatrix} \tag{81}$$

where the subscript v is introduced to differentiate the reduced order in Voigt notation.

$$\boldsymbol{\sigma}_v' = \tilde{\boldsymbol{K}}_v' \left[\boldsymbol{\varepsilon}_v' - \Delta T \boldsymbol{\alpha}_v'\right] \tag{82}$$

or

$$\begin{bmatrix} \sigma_{11}' \\ \sigma_{22}' \\ \sigma_{33}' \\ \sigma_{23}' \\ \sigma_{13'} \\ \sigma_{12}' \end{bmatrix} = \begin{bmatrix} K_{11}' & K_{12}' & K_{13}' & K_{14}' & K_{15}' & K_{16}' \\ \cdot & K_{22}' & K_{23} & K_{24} & K_{25} & K_{26} \\ \cdot & \cdot & K_{33}' & K_{34}' & K_{35}' & K_{36}' \\ \cdot & \cdot & \cdot & K_{44}' & K_{45}' & K_{46}' \\ \cdot & \cdot & \cdot & \cdot & K_{55}' & K_{56}' \\ \cdot & \cdot & \cdot & \cdot & \cdot & K_{66}' \end{bmatrix} \left(\begin{bmatrix} \varepsilon_{11}' \\ \varepsilon_{22}' \\ \varepsilon_{33}' \\ 2\varepsilon_{23}' \\ 2\varepsilon_{13}' \\ 2\varepsilon_{12}' \end{bmatrix} - \Delta T \begin{bmatrix} \alpha_1' \\ \alpha_2' \\ \alpha_3' \\ 0 \\ 0 \\ 0 \end{bmatrix} \right) \tag{83}$$

The stress vector, $\boldsymbol{\sigma}_v'$, can now be used to fill out the stress tensor, $\boldsymbol{\sigma}'$. Next, a rotation matrix, $\boldsymbol{C}$, is required to get the stress tensor from the material coordinate system to the problem coordinate system.

$$\tilde{\boldsymbol{\sigma}} = \tilde{\boldsymbol{C}}^T \tilde{\boldsymbol{\sigma}}' \tilde{\boldsymbol{C}} \tag{84}$$

In *CHAR*, the approach will be to use Eqns. (82) and (84) to define the stress tensor for integration of the PDEs.

IX.B. Finite-Element Formulation

The Galerkin weak statement for the equations can be developed using Eqn. (76). The equation is multiplied by a suitable test function, v, and integrated over the domain, Ω, while integrating the first term by parts to give the natural boundary condition term. The weak statement is then: Find $\boldsymbol{u} \in H^1$ such that

$$\int_\Omega \boldsymbol{\nabla} v \cdot \boldsymbol{\sigma}_d d\Omega - \int_\Omega v f_d d\Omega - \int_\Gamma v \left(\boldsymbol{\sigma}_d \cdot \hat{\boldsymbol{n}}\right) d\Gamma = 0 \quad \forall v \in H_0^1 \quad \text{for } d = 1,2,3 \tag{85}$$

The finite-element approximation to Eqn. (85) can be reached by expanding the independent variables and test functions in terms of a finite dimensional basis

$$\left(u_d\right)_h (\boldsymbol{x}) = \sum_{j=1}^{N} \left(u_d\right)_j \psi_j (\boldsymbol{x}) \tag{86}$$

$$\boldsymbol{\nabla}\left(u_d\right)_h (\boldsymbol{x}) = \sum_{j=1}^{N} \left(u_d\right)_j \boldsymbol{\nabla}\psi_j (\boldsymbol{x}) \tag{87}$$

$$v_h (\boldsymbol{x}) = \sum_{i=1}^{N} v_i \psi_i (\boldsymbol{x}) \tag{88}$$

$$\boldsymbol{\nabla} v_h (\boldsymbol{x}) = \sum_{i=1}^{N} v_i \boldsymbol{\nabla}\psi_i (\boldsymbol{x}) \tag{89}$$

where the subscript h is introduced to denote a finite dimensional approximation. Now, the unknowns are no longer functions of $\boldsymbol{x}$. Since the equation system should be satisfied for all combinations of nodal test function coefficients, v_i, their choice is arbitrary. Choosing a unique combination for each node allows for the development of a linear system where the number of equations equals the number of unknowns. In typical finite-element fashion, the coefficients are chosen to be $v_i = \delta_{il}$ for the l^{th} nodal equation. Consequently the nodal residual equations can now be written as

$$\int_\Omega \boldsymbol{\nabla}\psi_i \cdot \boldsymbol{\sigma}_d d\Omega - \int_\Omega \psi_i f_d d\Omega - \int_\Gamma \psi_i T_d d\Gamma = 0 \quad \text{for } d = 1,2,3 \tag{90}$$

for i = 1,2,...,N. The surface traction is defined as

$$T_d = \boldsymbol{\sigma}_d \cdot \hat{\boldsymbol{n}} \qquad \text{for } d = 1,2,3 \tag{91}$$

IX.C. Example Thermoelastic Problem: Bimetallic Strip

Bimetallic strips consist of two long, thin strips of differing metals bonded together. Since the two metals have different coefficients of thermal expansion, thermal stresses will cause the strip to bend as the bimetallic strip heats up. Bimetallic strips can be found in many devices such as clocks, thermostats, thermometers, lamp flashers, and time-delay relays. The operation of a bimetallic strip can be simulated using the one-way coupled thermal and thermoelastic solvers in *CHAR*.

Consider a bimetallic strip of two materials with identical thermal and elastic properties, but two different coefficients of thermal expansion. Metal A is on the bottom half of the strip and metal B is on the top half. Each metal half is $0.0005\,\mathrm{m}$ thick, $0.005\,\mathrm{m}$ wide, and $0.1\,\mathrm{m}$ long. The strip is cantilevered at one end and free to move elsewhere. There is no external loading on the strip. However, there is a constant heat flux of $20\,\mathrm{W/cm^2}$ applied to the cantilevered end. A schematic of the problem can be seen in Figure 22 and the problem parameters can be found in Table 6. The solution to the problem at every second from 0 to $10\,\mathrm{sec}$ can be seen in Figure 23 where the displacement is multiplied by 10 for visualization purposes. As expected, the strip bends towards material A so that the larger expansion can be accommodated in material B.

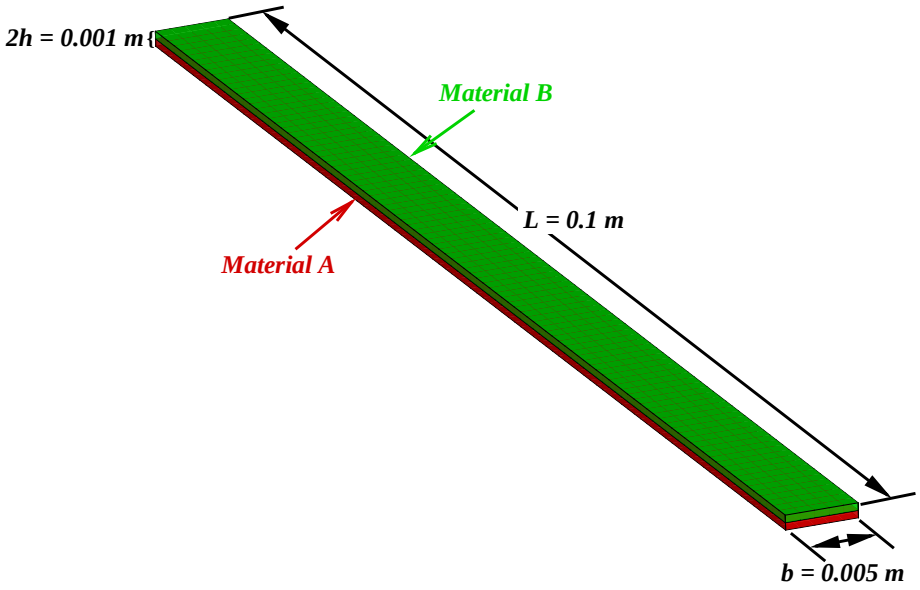

Figure 22. Schematic of bimetallic strip geometry.

Table 6. Bimetallic strip problem parameters.

$$
\begin{aligned}
E &= 200\,\mathrm{GPa} \\
\nu &= 0.3 \\
\alpha_A &= 1 \times 10^{-5}\,{}^{\mathrm{m}}/_{\mathrm{m\cdot K}} \\
\alpha_B &= 2 \times 10^{-5}\,{}^{\mathrm{m}}/_{\mathrm{m\cdot K}} \\
L &= 0.1\,\mathrm{m} \\
b &= 0.005\,\mathrm{m} \\
h &= 0.0005\,\mathrm{m} \\
\dot{Q} &= 2 \times 10^{6}\,{}^{\mathrm{W}}/_{\mathrm{m}^3} \\
C &= 500\,{}^{\mathrm{J}}/_{\mathrm{kg\cdot K}} \\
k &= 100\,{}^{\mathrm{W}}/_{\mathrm{m\cdot K}} \\
\rho &= 1000\,{}^{\mathrm{kg}}/_{\mathrm{m}^3} \\
T_o &= 300\,\mathrm{K}
\end{aligned}
$$

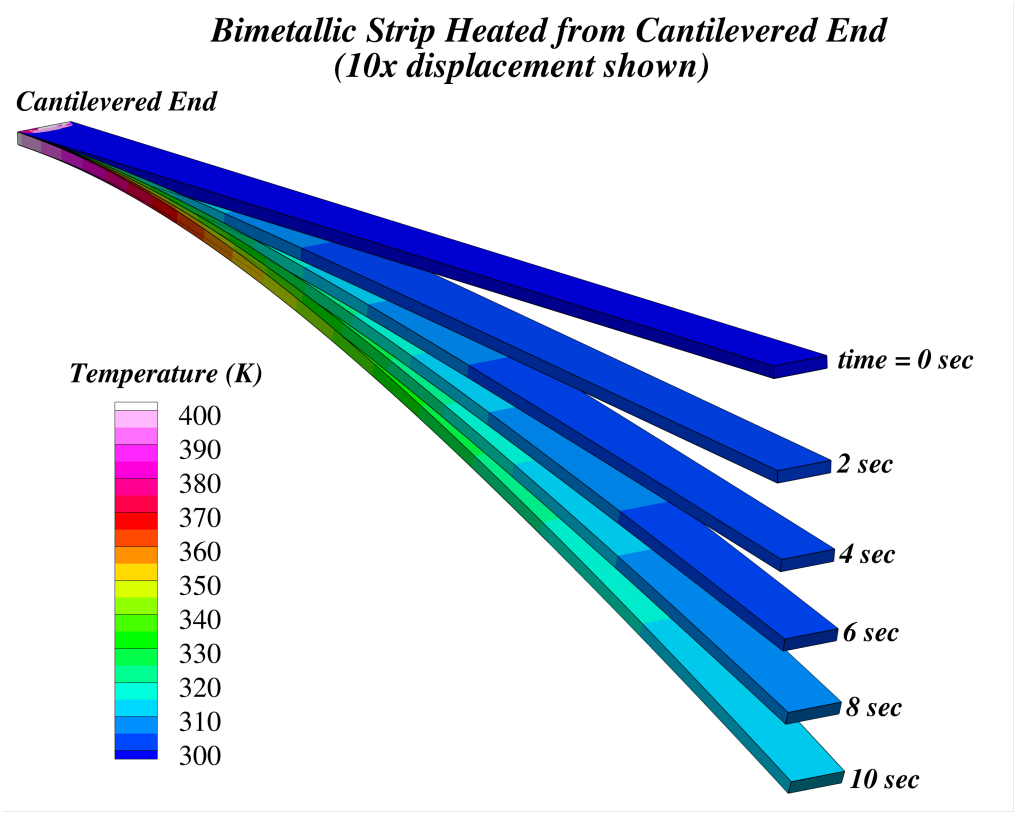

Figure 23. Solution to the bimetallic strip example problem (10× displacement shown).

X. Conclusions and Ongoing Development Efforts

The *CHAR* code has been developed to perform engineering design analysis of ablative TPS systems in one, two, and three dimensions. The physical models are at the macroscale level, which enables analysis of complete systems, but lacks the fidelity of micro and multi-scale modeling approaches. It is expected that higher fidelity models, such as those implemented in PATO,[1] can be used to identify relevant physics and develop appropriate macroscale models to be implemented in *CHAR*.

Model equations and demonstration cases have been presented for many of the physical models implemented in *CHAR* including porous flow, thermochemical ablation, contact modeling, mesh motion, adaptive mesh refinement, and thermoelasticity. While comparisons to data are presented, additional work must be done to fully validate *CHAR* for the broad class of charring ablation problems it is intended to solve.

Ongoing development efforts are intended to increase the modeling fidelity and improve the usability of the code. This includes

- Water phase change and transport modeling: This capability is necessary to model the phenomenon shown in Figure 12.
- Unsteady porous flow momentum equations: Implementation of unsteady porous flow momentum equations described by Weng[9] will allow for assessment of accuracy of assuming steady form of Darcy's law, which was done in this work. While solving the unsteady porous flow equations will likely be more accurate, using the steady form of Darcy's law is desirable since it reduces the coupled PDE count thereby reducing computational expense.
- Thermal non-equilibrium between solid and gas: Thermal non-equilibrium effects between the solid and gas could significantly impact the prediction of critical system performance such as substructure temperatures. Addition of separate solid and gas energy equations with an appropriate exchange term would be necessary to model this phenomenon. While implementation of such a modeling approach is feasible, it is not yet understood

how the modeling parameters would be informed, what the proper boundary conditions would be, and how model validation would be achieved.

- Chemical non-equilibrium modeling: The in-depth equilibrium of pyrolysis gases is likely not an appropriate assumption for all materials over all temperature and pressure regimes. Conservation equations for each gas species must be implemented with appropriate source terms to account for chemical reactions. Like the thermal non-equilibrium modeling, the chemical non-equilibrium modeling has similar challenges with informing modeling parameters and validating the model. This capability is also necessary for proper modeling of water transport.
- Mesh motion improvements: A robust and general mesh motion scheme is desired for the broad array of anticipated mesh topologies and deformations. Current effort is focused on the implementation of the boundary conditions developed by Droba.[17] Additionally, the development team intends to explore other PDE based methods for mesh motion and smoothing such as solving the bi-harmonic equation. Finally, other non-PDE based methods, such as the one presented by Luke et al.,[41] will also be investigated for speed and mesh quality under large deformations.
- Improving robustness of thermoelastic solver: Currently, the thermoelastic solver has only been used by the development team, and additional work is necessary to improve speed, robustness, and usability. Most notably, it has been observed that achieving converged linear system solutions is highly dependent on the choice of iterative linear system solver and preconditioning choices. Additionally, a wider variety of boundary conditions should be implemented before making this a production capability.
- Optimization: Since *CHAR* is intended to be used for production design work, it is beneficial to reduce computational expense as much as possible. To this point, minimal effort has been put into code optimization as the bulk of the development effort has focused on implementing and verifying new physical modeling capabilities. *CHAR* would greatly benefit from a thorough profiling effort to identify bottlenecks. Additionally, as larger problems are starting to be solved, memory management is becoming an issue. Effort should be put into reducing the memory footprint of the code.

XI. Acknowledgments

The authors would like to acknowledge everyone that has contributed to or enabled the development of the *CHAR* code and those that have contributed guidance when developing the content of this paper. This includes Jay LeBeau (NASA Johnson Space Center) Ben Blackwell (Sandia National Laboratories, retired), Micah Howard (Sandia National Laboratories), Nathan Calvert, Parul Agrawal (Analytical Mechanics Associates, NASA Ames Research Center), and Matt Maclean (CUBRC).

References

[1] J. Lachaud and N. N. Mansour. Porous-material analysis toolbox. *Journal of Thermophysics and Heat Transfer*, 28(2):191–202, 2014.

[2] Carl B. Moyer and Roald A. Rindal. An Analysis of the Coupled Chemically Reacting Boundary Layer and Charring Ablator, Part II: Finite Difference Solution for the In-Depth Response of Charring Materials Considering Surface Chemical and Energy Balances. Technical Report 66-7 Part II, Aerotherm, March 1967.

[3] F. S. Milos and Y.-K. Chen. Ablation, Thermal Response, and Chemistry Program for Analysis of Thermal Protection Systems. *Journal of Spacecraft and Rockets*, 50(1):137–149, 2013.

[4] F. S. Milos and Y.-K. Chen. Two-Dimensional Ablation, Thermal Response and Sizing Program for Charring Ablators. *Journal of Spacecraft and Rockets*, 46(6):1089–1099, 2009.

[5] Y.-K. Chen and F. S. Milos. Validation of a Three-Dimensional Ablation and Thermal Response Simulation Code. June 2009. AIAA Paper 2010-4645.

[6] John A. Dec. *Three Dimensional Finite Element Ablative Thermal Response Analysis as Applied to Heatshield Penetration Design*. PhD thesis, Georgia Institute of Technology, Atlanta, GA, March 2010.

[7] B.F. Blackwell. Numerical prediction of one-dimensional ablation using a finite control volume procedure with exponential differencing. *Numerical Heat Transfer*, 14(1):17–34, 1988.

[8] B.F. Blackwell and R. E. Hogan. One-dimensional ablation using landau transformation and finite control volume procedure. *Journal of Thermophysics and Heat Transfer*, 8(2):282–287, 1994.

[9] H. Weng and A. Martin. Multidimensional modeling of pyrolysis gas transport inside charring ablative materials. *Journal of Thermophysics and Heat Transfer*, 28(4):583–597, 2014.
[10] H. Weng and A. Martin. Numerical investigation of thermal response using orthotropic charring ablative material. *Journal of Thermophysics and Heat Transfer*, 29(3):429–438, 2015.
[11] H. Weng, S. C. C. Bailey, and A. Martin. Numerical study of iso-q sample geometric effects on charring ablative materials. *International Journal of Heat and Mass Transfer*, 80:570–596, 2015.
[12] G.C. April, R. W. Pike, and E.G. del Valle. Modeling reaction gas flow in the char layer of an ablator. *AIAA Journal*, 9(6):1113–1119, 1971.
[13] E.G. del Valle, R. W. Pike, and G.C. April. Transport phenomena in the char zone ii: Equilibrium composition of degradation products of ablation. *Symposium on the Technology of Ablation, American Institute of Chemical Engineers*, 1967.
[14] Adam Joseph Amar. Modeling of One-Dimensional Ablation with Porous Flow Using Finite Control Volume Procedure. Master's thesis, North Carolina State University, 2006.
[15] Brandon Oliver and Adam Amar. Inverse heat conduction methods in the *CHAR* code for aerothermal flight data reconstruction. June 2016. 46th AIAA Thermophysics Conference (submitted for publication).
[16] Giovanni Salazar, Justin Droba, Brandon Oliver, and Adam Amar. Development, verification, and validation of enclosure radiation capabilities in the charring ablator response (*CHAR*) code. June 2016. 46th AIAA Thermophysics Conference (submitted for publication).
[17] Justin Droba. Tangle-free finite element mesh motion for ablation problems. June 2016. 46th AIAA Thermophysics Conference (submitted for publication).
[18] Adam Amar, Nathan Calvert, and Benjamin Kirk. Development and Verification of the Charring Ablating Thermal Protection Implicit System Solver. January 2011. 49th AIAA Aerospace Sciences Meeting AIAA Paper 2011-144.
[19] Gaël Guennebaud, Benoît Jacob, et al. Eigen v3. http://eigen.tuxfamily.org, 2010.
[20] David G. Goodwin. Cantera c++ user's guide. Technical report, California Institute of Technology, October 2002.
[21] Benjamin S. Kirk, John W. Peterson, Roy H. Stogner, and Graham F. Carey. `libMesh`: A C++ Library for Parallel Adaptive Mesh Refinement/Coarsening Simulations. *Engineering with Computers*, 22(3):237–254, 2006.
[22] Satish Balay, Kris Buschelman, Victor Eijkhout, William D. Gropp, Dinesh Kaushik, Matthew G. Knepley, Lois Curfman McInnes, Barry F. Smith, and Hong Zhang. PETSc users manual. Technical Report ANL-95/11 - Revision 2.3.0, Argonne National Laboratory, April 2004.
[23] G. Karypis and V. Kumar. METIS unstructured graph partitioning and sparse matrix order. Technical report, University of Minnesota, Department of Computer Science, August 1995.
[24] P. J. Roache. *Verification and Validation in Computational Science and Engineering*. Hermosa Publishers, 1998.
[25] P. Knupp and K. Salari. *Verification of Computer Codes in Computational Science and Engineering*. Chapman & Hall/CRC, 2003.
[26] Benjamin S. Kirk. *Adaptive Finite Element Simulation of Flow and Transport Applications on Parallel Computers*. PhD thesis, The University of Texas at Austin, May 2007.
[27] J. N. Lyness. Numerical algorithms based on the theory of complex variable. 1967. In Proceedings of the ACM National Meeting (Washington D.C.), pp. 125-133.
[28] J. N. Lyness and C. B. Moler. Numerical algorithms based on the theory of complex variable. *SIAM Journal of Numerical Analysis*, 4(2):202–210, June 1967.
[29] Jochen Marschall and Michael E. Cox. Gas Permeability of Lightweight Ceramic Ablators. *Journal of Thermophysics*, 13(3):382 – 384.
[30] M. Utku and G. F. Carey. Boundary penalty techniques. *Computer Methods in Applied Mechanics and Engineering*, 30:103–118, 1982.
[31] R. M. Kendall. An analysis of the coupled chemically reactiing boundary layer and charring ablator, part v: A general approach to the thermochemical solution of mixed equilibirum-nonequilibrium , homogeneous and heterogeneous systems. Technical Report 66-7 Part V, Aerotherm, June 1968.
[32] Y.-K. Chen and F. S. Milos. Comprehensive Model for Multicomponent Ablation Thermochemistry. January 1997. AIAA Paper 97-0141.
[33] William Kays, Michael Crawford, and Bernhard Weigand. *Convective Heat and Mass Transfer*. McGraw-Hill, 4th edition, 2005.
[34] Daniel C. Reda, Francis C. Ketter, and Chien Fan. Compressible turbulent skin friction on rough and rough/wavy walls in adiabatic flow. 7th AIAA Fluid and Plasma Dynamics Conference, AIAA Paper 1974-574, June 1974.
[35] T. J. Dahm et al. Passive nosetip technology (pant ii) program. Technical Report SAMSO-TR-11, Acurex Corporation, October 1976.

[36] M. L. Finson. A model for rough wall turbulent heating and skin friction. 20th AIAA Aerospace Sciences Meeting, AIAA Paper 1982-0199, January 1982.
[37] J. Dolbow and I. Harari. An efficient finite element method for embedded interface problems. *International Journal for Numerical Methods in Engineering*, 78:229–252, 2009.
[38] J. A. Nitsche. Über ein Variationsprinzip zur Lösung von Dirichlet-Problemen bei Verwendung von Teilräumen, die keinen Randbedingungen unterworfen sind. Abhandlungen ausdem Mathematischen Seminar der Universität Hamburg 36, 9-15, 1970/71.
[39] Parul Agrawal, Donald T. Ellerby, Matthew R. Switzer, and Thomas H. Squire. Multidimensional testing of thermal protection materials in the arcjet test facility. June 2010. 10
textsuperscriptth AIAA/ASME Joint Thermophysics and Heat Transfer Conference, AIAA Paper 2010-4664.
[40] Michael J. Wright, Graham V. Candler, and Deepak Bose. Data-Parallel Line Relaxation Method for the Navier-Stokes Equations. *AIAA Journal*, 36:1603–1609, 1998.
[41] Edward Luke, Eric Collins, and Eric Blades. A fast mesh deformation method using explicit interpolation. *Journal of Computational Physics*, 231(2):586–601, 2012.